

UNIVERSITY OF PAVIA

Department of Electrical, Computer, and Biomedical Engineering

**ANALOG FRONT-END CIRCUITS
FOR HIGHLY INTEGRATED
ULTRASOUND IMAGING SYSTEMS**

Advisor:
Prof. Mazzanti Andrea

Ph.D. Thesis of:
Sautto Marco

XXIX Cycle

Contents

Introduction	5
Chapter 1. System Overview	9
1.1. Physical Principles	9
1.2. Ultrasound Imaging	13
1.3. CMUT Description	20
1.4. CMUT Non Linear Model	22
Chapter 2. RX Amplifiers Comparison	27
2.1. RX amplifiers and pulse-echo frequency response.	28
2.2. Noise Analysis	33
Chapter 3. A Transceiver Front-End Design	39
3.1. RX amplifier	40
3.2. TX Driver	42
3.3. T/R Switch	44
3.4. Experimental Results	46
Chapter 4. CMUT Second Harmonic Compensation	57
4.1. Linearization Technique	58
4.2. High-Voltage Tunable Pulser	60
4.3. Experimental Results	62
Chapter 5. PGA Design for Time-Gain Compensation	65
5.1. PGAs: Requirements and Limitations	66
5.2. Cross-Coupled Pair Regeneration: Theory	69

5.3. PGA Design Exploiting the XCP Regeneration	77
5.4. Experimental Results	82
Chapter 6. Conclusions	87
Bibliography	89

Introduction

Ultrasound imaging is a well-established medical diagnostic technique. Compared with other imaging modalities, such as for example X-ray, ultrasound is harmless to the patient and less expensive while providing real-time imaging capability with adequate resolution for most applications. Piezoelectric materials have dominated the ultrasound transducers technology for a long time but, thanks to the intense research activity in recent years, capacitive micromachined ultrasonic transducers (CMUT) are emerging as a competitive alternative for next generation imaging systems. They offer wide bandwidth, improving resolution, and a wider operating temperature range [1, 2]. Moreover, the MEMS fabrication process allows for high design flexibility, reproducibility, compact size and low cost. These features, paired with an easier integration with the electronic front-end, make CMUT attractive for new imaging systems such as 3D real-time scanners leveraging dense matrices of transducers [3, 4] and portable ultrasound imagers, an emerging class of devices which is rapidly expanding and is expected to have a broad market potential [5–7].

The development of optimized transducers as well as highly integrated front-end electronic interfaces is an active area of research [8–11]. Compact size, i.e. high integration, low power and high dynamic range are key design targets to enable a widespread deployment of future CMUT-based imaging systems [12].

The main issue in IC design for ultrasound transducers is the co-existence of high-voltage drivers in the transmit path along with low-voltage and low-noise circuits in the receiver. Device stacking in low-voltage technologies has been investigated to deliver up to 10-20V TX pulses [13, 14]. However CMUTs must be driven at 100 V or more to achieve acoustic pressure comparable with piezoelectric transducers [1], mandating the use of high-voltage technologies [15–17]. Moreover, CMUTs show high equivalent source impedance leading to high sensitivity of the output SNR to the loading capacitance [18]. Co-design of the TX and RX circuits and possibly integration on the same die are key to minimize the overall parasitic capacitance and achieve performance competitive with piezoelectric transducers. In this framework, the BCD-SOI technology is particularly attractive, providing high-voltage and high-speed devices simultaneously [19, 20].

The objective of the thesis is to analyze the ultrasound system, when a CMUT is used instead of a piezoelectric transducer, to identify and design the best integrated solution to optimize the front-end performance. After giving an overview of the ultrasound system and the Capacitive Micromachined Ultrasonic Transducer (CMUT) in Chapter 1, Chapter 2 presents a thorough comparison between RX amplifier alternatives. Then, Chapter 3 proposes the design of a CMUT front-end circuits comprising a TX driver, T/R switch and RX amplifier [21, 22]. Realized in BCD8-SOI technology from STMicroelectronics, the TX delivers up to 100V pulses, while the RX shows 70dB dynamic range with very low noise at 1mW only power dissipation. Measurement results and imaging experiments are presented and discussed. In Chapter 4, the non-linear behavior of the CMUT is discussed and possible solution

proposed. Experimental results demonstrate a significant reduction of the second-harmonic distortion, estimated to be lower than -30 dB, resulting in good linearization for typical nonlinear imaging operation. In addition, Chapter 5 shows a novel amplifier architecture exploiting the regeneration feature of the cross-coupled pair [23]. It will be used as Programmable Gain Amplifier (PGA) in the ultrasound chain. A test-chip in $0.18\mu\text{m}$ CMOS provides 15dB to 66dB gain over 50MHz bandwidth. With state-of-the art noise and linearity performance, a record GBW up to 100GHz is demonstrated with only $420\mu\text{W}$ power dissipation. Conclusions are drawn in Chapter 6.

CHAPTER 1

System Overview

Ultrasound imaging has been a major medical diagnostic imaging technique for decades. Internal organs can be seen thanks to the echoes of ultrasound waves generated by the probe, so it is useful to introduce some physical concepts to clarify the operation of Ultrasound Imaging devices. Then the State of the Art of Ultrasound Imaging will be presented.

1.1. Physical Principles

Ultrasound waves are acoustic waves with frequencies greater than 20 kHz, which makes them inaudible. The frequencies of ultrasound waves used for human tissue imaging normally range from 1 MHz to 20 MHz, according to the target organs and the wanted resolution. The sound speed is supposed constant and generally equal to 1540 m/s though it may change with the target tissue density [24].

For imaging to take place, the probe must be put in contact with the patient's skin. In phase 1, the transmission phase, the probe -or better, the probe transducers- acts as a source of acoustic waves. The waves will then propagate in the patient's body, where attenuation, reflection and refraction phenomena take place, generating echoes. In phase 2, the receiving phase, the probe acts as a receiver for the echoes. Before an echo can be received, it is necessary to wait for the acoustic wave to get to the interface and for the generated echo to travel back to

the probe. The distance of the reflecting interface is then determined by the device through the “range equation” [25]:

$$(1.1.1) \quad z = \frac{c t}{2}$$

where z is the distance being measured, c is the speed of sound and t is the elapsed time between the emission of the wave and the reception of the generated echo. The concept of acoustic impedance is helpful to further understand the operation of Ultrasound Imaging devices. Acoustic impedance is a characteristic parameter of a medium: it is a complex number representing the ratio of the acoustic pressure to the vibration speed of particles at a certain point in space and it is equal to

$$(1.1.2) \quad Z_m = \rho c \left[\frac{\text{kg}}{\text{m}^2\text{s}} \right]$$

where ρ is the medium density expressed in $\left[\frac{\text{kg}}{\text{m}^3} \right]$ and c is the propagation speed of the acoustic wave in the medium expressed in $\left[\frac{\text{m}}{\text{s}} \right]$ [26]. Therefore, if the medium in which the wave is traveling is not homogeneous, which implies that it is not characterized by just one density value, its acoustic impedance will not be constant. When the wave encounters the discontinuity that causes the acoustic impedance of the medium to change, part of the energy brought by the wave is reflected and the rest is refracted, as shown in Fig. 1.1.1. The direction of the reflected wave depends on that of the incident wave: actually, the angle of reflection θ_r is equal to the angle of incidence θ_i , which is the

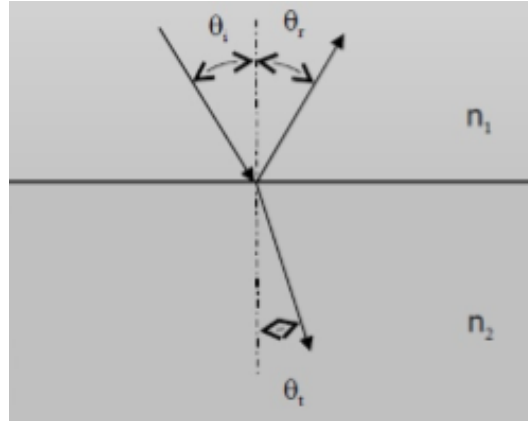


Figure 1.1.1. Snell law.

angle between the incident wave front and the normal to the discontinuity plane. On the other hand, refraction is governed by Snell's law, according to which

In the ideal case, where an acoustic wave crosses a planar interface between two media with no air bubbles in the middle, the reflected percentage of the incident energy and the refracted percentage are represented by the reflection coefficient R and the transmission coefficient T [24].

$$(1.1.3) \quad \frac{n_1}{n_2} = \frac{\sin(\theta_i)}{\sin(\theta_t)}$$

where n_1 and n_2 are the refractive indexes of the two portions of the medium and θ_t is the transmission angle of the wave in the second portion of the medium. Normal incidence produces both a null reflection angle and a null refraction angle.

$$(1.1.4) \quad R = \frac{P_r}{P_i} = \frac{Z_2 \cos(\theta_i) - Z_1 \cos(\theta_t)}{Z_2 \cos(\theta_i) + Z_1 \cos(\theta_t)}$$

Table 1.1.1. ACOUSTIC IMPEDANCES OF DIFFERENT TYPES OF HUMAN TISSUE

Substance / Tissue	$Z_m \left[10^6 \frac{\text{kg}}{\text{m}^2\text{s}} \right]$
Air at 20°C	0.000444
Water at 20°C	1.43
Fat	1.34
Liver	1.64
Blood	1.65
Muscle	1.7
Bone	3.75 - 7.38

$$(1.1.5) \quad T = \frac{P_t}{P_i} = \frac{2Z_2 \cos(\theta_i)}{Z_2 \cos(\theta_i) + Z_1 \cos(\theta_t)}$$

where Z_1 and Z_2 are the acoustic impedance of the two media.

Table 1.1.1 shows the value of the acoustic impedance of some substances and some types of human tissue.

Since the operation of Ultrasound Imaging relies on the reception of reflected echoes, to see internal organs part of the acoustic wave's energy must be reflected and part of it transmitted at each interface between different tissues. As eq. (1.1.4) shows, the more Z_1 and Z_2 differ the higher is the reflection coefficient: in some cases, like that of a Muscle-to-Bone interface, the reflection coefficient R gets very close to 1 resulting in an almost null transmission. This is why it is impossible to see through bones with Ultrasound Imaging. Also, diseases affecting hollow organs like the stomach and the intestines cannot be diagnosed this way as these organs are full of air, which has a very low acoustic impedance resulting in very low transmission.

Another drawback of Ultrasound Imaging is due to wave amplitude attenuation in the human body. The wave amplitude undergoes an exponential reduction with the traveled distance, according to this law [25]:

$$(1.1.6) \quad P(z) = P_0 e^{-\alpha z}$$

where P_0 is the reference pressure at a certain point in space, $P(z)$ is the pressure at a distance equal to z units from the point where the pressure is P_0 and α is the attenuation coefficient. α is roughly $1 \frac{\text{dB}}{\text{MHz cm}}$ for the human body. The attenuation coefficient is strongly dependent on frequency and grows substantially with a small frequency growth. The system resolution, which is the dimension of the smallest detail that can be distinguished with the Ultrasound Imaging device, grows with the working frequency too. This sets a tradeoff between the imaging resolution and the imaging depth.

1.2. Ultrasound Imaging

Ultrasound Imaging has been an important medical diagnostic imaging technique for several decades. At the beginning of its history, in the early Fifties, the available imaging was one-dimensional -Amplitude mode- as the probe was equipped with one transducer only. The images available showed the interfaces crossed by the wave in the direction pointed by the beam and were oscilloscope-like [25].

In the late Fifties, a new operating mode replaced the Amplitude mode: it is the Brightness mode, with which the reflecting interfaces are represented as brighter regions on the black screen. Then doctors

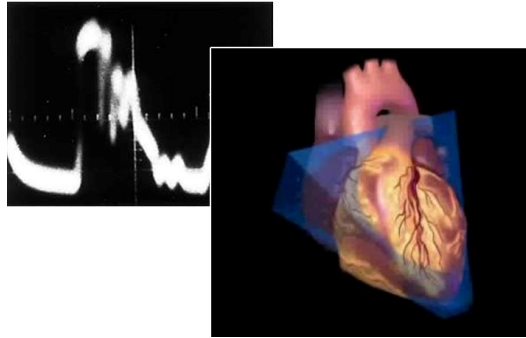


Figure 1.2.1. A-mode picture from the Fifties on the left and recent 3D image on the right.

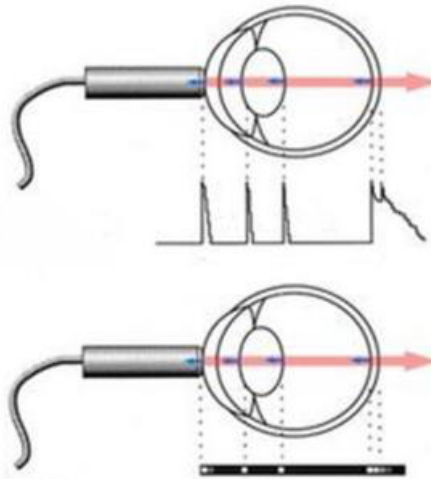


Figure 1.2.2. A-mode imaging principle (above) and B-mode imaging principle (below).

started to dispose of two-dimensional black and white static images thanks to the scanning of a plane of the patient's body through a mechanical steering of the ultrasound beam. In the Sixties, linear arrays of transducers appeared in the probe: ultrasound images were now real time and two-dimensional. After 2000, 3D images started being available, first static then real time. Fig. 1.2.1 and 1.2.2 show how the images provided by this kind of technique have changed through time

Ultrasound Imaging has many advantages: first of all it is a non-invasive technique, as well as one that doesn't expose the patient to ionizing radiation, as opposed to X-ray imaging. Moreover, the imaging device can be placed in any room -there are even portable devices- and no recovery time is required between two successive usages. Finally, it has a lower cost with respect to other imaging techniques, like Magnetic Resonance Imaging and Computed Axial Tomography, so it has a wider diffusion and allows preventive screening. Its main drawback with respect to alternative techniques is a lower resolution [25].

As said before, Ultrasound Imaging relies on the transmission of acoustic waves through a transducer -working as an actuator- and the reception of the echoes reflected by the patient's tissues through the same transducer -now working as a sensor. Usually the probe contains not one single transducer, but an array of them: in transmission mode, the electronics sets the delay with which the excitation pulses get to each transducer in order to steer the beam in a different direction, just like in electromagnetic phased arrays, in order to scan the whole organ section [25]. This concept is called "beamforming" and is also employed in receiving mode for correct focusing, as echoes coming from a certain point in the patient's body reach each transducer with a different delay. This delay needs to be compensated for by the electronics. Figure 1.2.3 shows beamforming in transmission mode while Figure 1.2.4 in receiving mode. 3D images have been possible thanks to the idea of making probes with a matrix of transducers instead of just an array, as shown in Figure 1.2.5 [25].

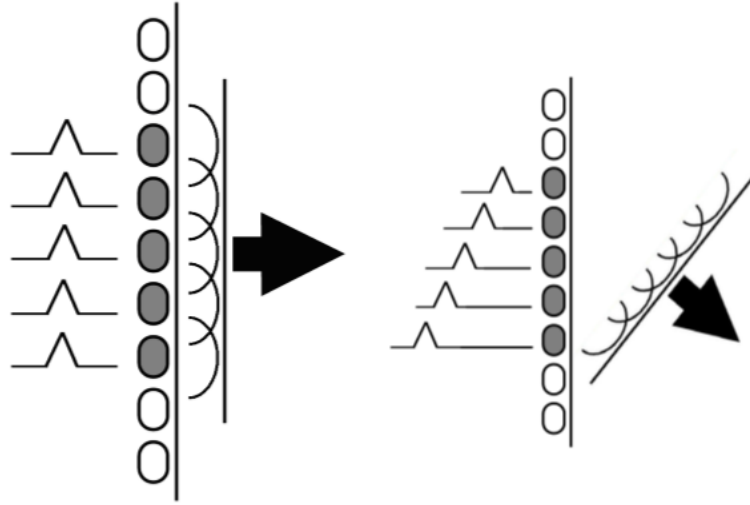


Figure 1.2.3. Beamforming in transmission mode.

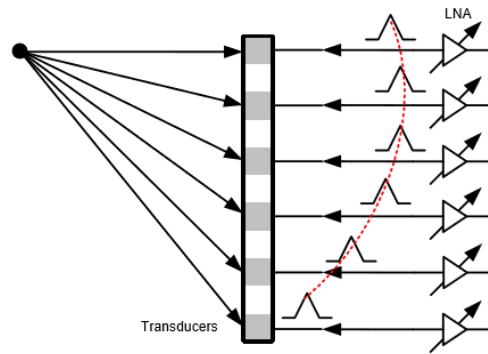


Figure 1.2.4. Beamforming in receiving mode.

Figure 1.2.6 presents the many blocks inside a standard Ultrasound Imaging System. In transmission mode, the signal follows the transmitter chain path, while in receiving mode it follows the receiver chain one.

- (1) The Console is a computer that acts as a user interface and processes the images.
- (2) The Display shows the images produced by the Console.
- (3) The TX Beamformer is a digital block that carries out the beamforming in transmission mode, as explained before.

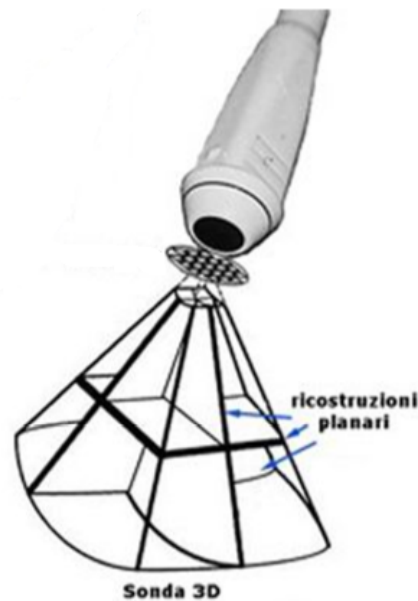


Figure 1.2.5. Probe with a matrix of transducers.

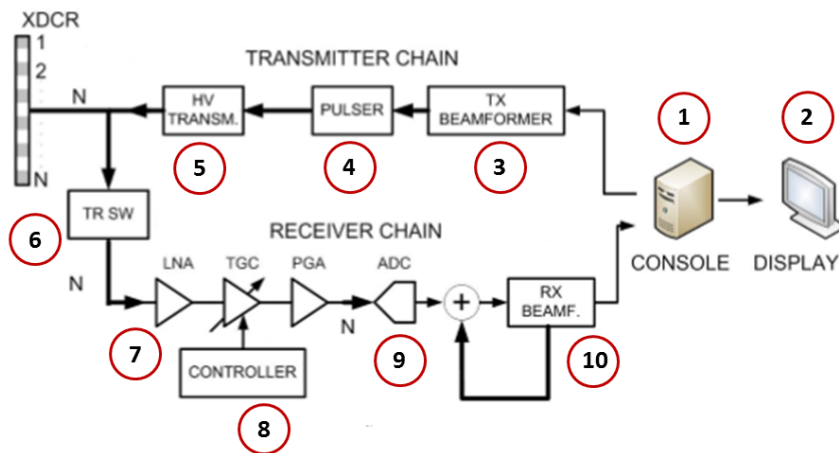


Figure 1.2.6. Block representation of a standard Ultrasound Imaging system.

- (4) The N Pulsers generate the pulses that drive the High Voltage (HV) Transmission circuitry; they are generally Low Voltage (LV) circuits.
- (5) The N High Voltage Transmission blocks drive the N transducers. Often blocks 4 and 5 are merged. HV switching matrices

could be placed after this block in order to send the same signal to several transducers.

- (6) The N T/R Switches protect the LV Receiver chain as the Transmitter and the Receiver chains are both connected to the probe. During the transmission phase, the transducers are driven with very high voltages, which would instantly break the LV receiving circuitry if they reached it. So during the transmission phase the T/R Switch disconnects the Receiver chain from the probe, while at the beginning of the receiving phase it reconnects it.
- (7) The N Low Noise Amplifiers receive the echoes and amplify them adding the lowest possible noise.
- (8) The N Time Gain Control and Programmable Gain Amplifier blocks condition the received signal, compressing its dynamic range and relaxing the specifications of the following Analog to Digital Conversion stage.
- (9) The N Analog to Digital Converters receive the suitably conditioned LNA analog output signals and convert them into digital.
- (10) The RX Beamformer block superimposes the digital signals coming from the ADCs to correctly reconstruct the image.

These blocks can be gathered in three groups:

- The Analog Front End (AFE) includes blocks from 4 to 8;
- The Beamformer and digital Frontend includes blocks 3, 9 and 10;
- The Backend includes blocks 1 and 2.

Most of the Ultrasound systems currently in use consist of a bulky machine containing all the circuitry needed to run the probe. The probe is connected to the machine through a number of coaxial cables equal to the number of transducers, which limits the maximum number of transducers. Moreover, since the transducers must be driven at a voltage higher than 100 V, the coaxial cables connecting the transmitter chain to the probe must be perfectly shielded to avoid dangerous couplings. On the other hand, the received echoes have a much lower amplitude -of the order of hundreds of microVolts- so the receiving chain must include very sensitive LNAs. Finally, the cables that connect the probe to the machine are more than a meter long but must assure a very low signal attenuation. To improve the quality of the produced images and enable 3D real time imaging, thousands of transducers must be integrated on the probe. Therefore, the AFE has to be integrated in the probe: this way the signals reaching the probe during the transmission phase are LV, as the HV circuits are in the probe itself, while in the receiving phase the signals coming from the transducers are strengthened before traveling on the cables. This releases the constraints on the cables.

In the following chapters, analysis and techniques to integrate the HV and LV analog front end circuits on the same die will be shown. A set of circuits has been designed to enable the future development of a fully integrated ultrasound probe. To make it possible the chosen technology is the BCD-SOI from STMicroelectronics -more on this in the following chapters.

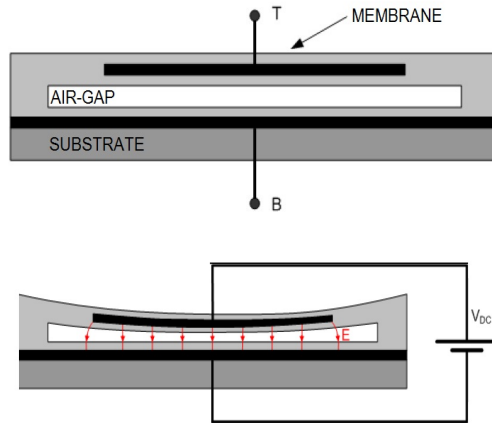
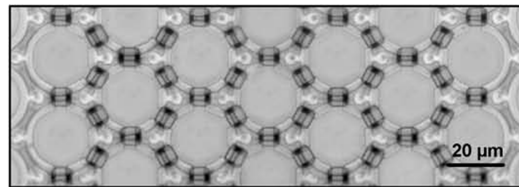
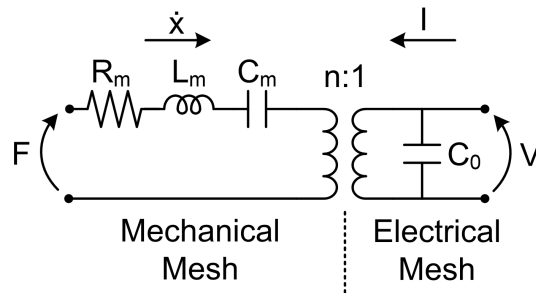


Figure 1.3.1. CMUT simplified cross-section.



a)



b)

Figure 1.3.2. Microphotograph of the CMUT transducer and equivalent electro-mechanical circuit model.

1.3. CMUT Description

The CMUT is an electro-acoustic transducer consisting of an array of capacitors, each one realized with a thin flexible plate suspended above a substrate (Fig. 1.3.1). To transmit acoustic power, the plate can be made to vibrate by applying a time-varying voltage between the two capacitor electrodes. Conversely, when the transducer is used

Table 1.3.1. COMPONENTS VALUE OF THE CMUT EQUIVALENT CIRCUIT MODEL

R_m	500 m Ω
C_m	27.5 nF
L_m	3.5 nH
C_0	9.2 pF
n	0.01

to detect the acoustic pressure, the incident wave causes vibrations of the plate and variation of the equivalent capacitance. The front-end presented in this work is designed for a CMUT array comprising 192 transducers elements, provided with their own individual electrodes, and sharing one common electrode. A microphotograph of a small part of a transducer element, realized with 637 circular cells of 29.6 μ m diameter in parallel is shown in Fig. 1.3.2(a). Width and length of the single element are 200 μ m and 3 mm respectively. The detailed geometry of the single CMUT cell, i.e the diameter and thickness of the plate, the gap height, as well as the microfabrication process, packaging technology and probe assembly are described in [1] and [2]. The transducer was designed for pulse-echo operation using receive voltage readout, with a 12MHz center frequency and a -6dB fractional bandwidth greater than 100% when biased at 220 V.

The equivalent circuit in Fig. 1.3.2(b) is commonly adopted to model the electro-mechanical operation of the transducer, linearized around a bias point [27]. This circuit will be used in the first part of the thesis to study the effect of the receiver architecture on the system transfer function. The circuit is a two-port network composed of two sides coupled by a transformer, which mimics the electro-acoustic

energy conversion of the transducer. C_0 and n are proportional to the CMUT area, while C_m , L_m , R_m are inversely proportional [28]. The effect of the electrostatic nonlinearity on the small signal behavior, i.e. the spring-softening effect [29], is lumped in C_m .

A common figure of merit is the electromechanical conversion factor, normalizing the mechanical energy to the total energy: $k_T^2 = \frac{E_{mech}}{E_{mech} + E_{elec}} = \frac{n^2 C_m}{n^2 C_m + C_0}$ (being E_{mech} and E_{elec} the mechanical and electrical energy respectively) [30].

The transducer shows best performance, i.e. maximum transmit efficiency and receive sensitivity, when the plate is inflected with high DC bias voltage applied between the CMUT electrodes [30]. The component values of the equivalent circuit model, estimated through finite element simulations and measurements of the CMUT biased at 270 V are reported in Table 1.3.1. The electromechanical conversion factor is 0.23.

1.4. CMUT Non Linear Model

High-voltage driven CMUTs [31] behave nonlinearly due to the nonlinear relationship between the applied voltage and the generated electrostatic force. Under this condition the equivalent circuit shown in Fig. 1.3.2(b) is no more valid. The behavior of a CMUT can only be analyzed precisely by means of the Finite Element Analysis. This method is impractical. To better understand where the non-linear behavior originates, the parallel-plate capacitor approximation is exploited to extract a model that can easily be utilized by a designer. With this approximation the bending of the membrane is neglected and the transducer is considered equivalent to a mass-spring-damper system as the one presented in Fig. 1.4.1.

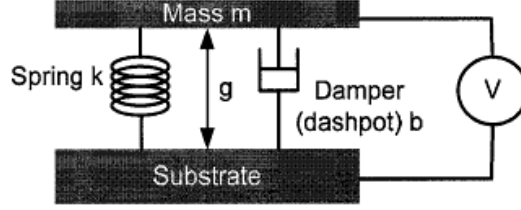


Figure 1.4.1. CMUT mass-spring-damper model.

When an electrostatic force is applied to the membrane it bends downwards exerting a force directed upwards. This force tends to bring the system back to equilibrium so it can be modeled with a spring. All losses are modeled with one single dissipative element (the damper). The complete model includes the two electrodes, a rigid mass (m) representing the membrane, a gap (g) between the substrate and the membrane, a spring with an elastic constant k and a damper with a damping factor b . A voltage V is applied between the electrodes [27].

Applying Newton's second law:

$$(1.4.1) \quad m\ddot{x} = m\ddot{g} = \sum F = F_e + F_m + F_s + F_b$$

where $x = g - g_0$ and g_0 is the initial distance, F_e is the electrostatic force, F_m is the mechanical force applied through the propagation medium, F_s is the elastic force and F_b is the force exerted by the damper.

$$(1.4.2) \quad F_s = -kx$$

$$(1.4.3) \quad F_b = -b\dot{x} = -b\nu$$

$$(1.4.4) \quad F_e = -\frac{\varepsilon_0 A V^2}{2g^2}$$

Therefore

$$(1.4.5) \quad m\ddot{x} + b\dot{x} + kx = F_e + F_m$$

where ν is the membrane speed, ε_0 is the vacuum permittivity and A is the membrane area. As first order approximation, $b = Z_m$ is the acoustic impedance of the medium. Correction factors to account for a non-rigid membrane may be added while other phenomena like spring softening and higher order vibrational modes are usually neglected.

It is interesting to link the Mason Model in Fig. 1.3.2 to the parallel-plate capacitor approximation in eq. (1.4.5). Applying the Kirchhoff's voltage law to the mechanical mesh:

$$(1.4.6) \quad F - nV = R_m \dot{x} + s L_m \ddot{x} + \frac{1}{s C_m} \dot{x}$$

since \dot{x} is modeled as a current, it can be expressed as the derivative of the charge q flowing into the mechanical mesh:

$$(1.4.7) \quad \dot{x} = \frac{dq}{dt}$$

thus, eq. (1.4.6) can be rewritten

$$(1.4.8) \quad F - nV = s R_m q + s^2 L_m \dot{q} + \frac{q}{C_m}$$

Applying the Laplace inversion theorem and assuming null initial condition

$$(1.4.9) \quad F - nV = \frac{q}{C_m} + R_m \dot{q} + L_m \ddot{q}$$

Comparing eq. (1.4.5) with eq. (1.4.9), the mass-spring-damper model can be related to the equivalent circuit as shown below:

$$(1.4.10) \quad q = x$$

$$(1.4.11) \quad F_m = F$$

$$(1.4.12) \quad F_e = -nV$$

$$(1.4.13) \quad L_m = m$$

$$(1.4.14) \quad C_m = \frac{1}{k}$$

$$(1.4.15) \quad R_m = b$$

To obtain the classical Mason Model, the previous equations are linearized around the fixed biasing voltage of the CMUT (≈ 200 V in this case). This approximation is accurate during the RX phase, when the received signal amplitude is negligible compared to 200 V. During the TX phase, the high voltage pulses applied to the membrane make the CMUT behave non linearly, so higher harmonics are generated. Equation (1.4.4) demonstrates the highly non-linear CMUT conversion from force to voltage and vice versa.

CHAPTER 2

RX Amplifiers Comparison

Optimization of the receiving circuits is a fundamental task to achieve a high integration level. This cannot be performed without a co-design of the mechanical transducer and the receiving (RX) amplifier. Minimizing the RX current consumption is fundamental to improve the overall power efficiency because the transducer is used to receive the backscattered echoes for most of the time, pushing investigation of the optimal RX amplifier. Several alternatives have been proposed so far. The most common approach is a trans-resistance amplifier [9, 10, 18, 32–36] but capacitive-feedback amplifiers [8, 37, 38] and high input impedance stages [39, 40] (i.e. voltage amplifiers) have been proposed as well. Nevertheless, a rigorous comparison between the three alternatives, aimed at identifying differences and the most convenient approach is missing.

The CMUT RX interface circuit has to detect the capacitance variations generated by the impinging acoustic waves. In view of integration of large arrays, the power budget for each receiver may be very small. At the same time, high SNR and dynamic range are critical not to compromise image quality. Different RX amplifier configurations have been proposed for CMUTs. The amplifier configuration has a significant impact on the overall performance but a comparative discussion among different alternatives has not been reported in literature. The transfer function and input impedance (determining the transducer loading)

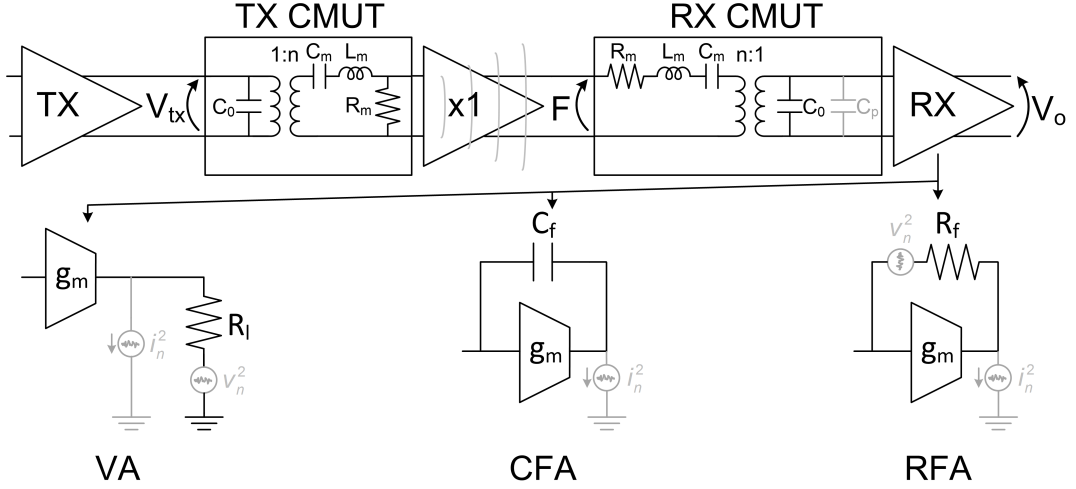


Figure 2.1.1. Block diagram adopted to simulate the pulse-echo response with different RX amplifier configurations.

affect the pulse-echo frequency response. Moreover, for a given power budget, the amplifier configuration has a remarkably different impact on the output SNR.

Following the description of the electro-acoustic characteristics of the transducer in section 1.3, this chapter compares the most popular CMUT RX amplifier configurations. The influence on the pulse-echo frequency response is analysed and the noise performance is compared in order to identify the most convenient solution to achieve best SNR for a given power budget.

2.1. RX amplifiers and pulse-echo frequency response.

To analyse the impact of the RX amplifier on the pulse-echo frequency response we consider the equivalent circuit depicted in Fig. 2.1.1 [28]. Two CMUTs are considered to model the roundtrip path. A transmitter drives the electrical side of the TX CMUT. The TX voltage, V_{tx} , is converted into a force delivered to the RX CMUT¹. An ideal

¹When excited by large TX voltage signals, the CMUT has a non-linear voltage-to-pressure response. Nonetheless, adoption of a linear CMUT TX model is justified

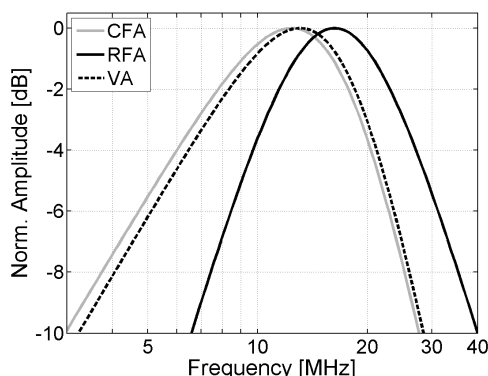


Figure 2.1.2. Simulated pulse-echo responses with different RX amplifier configurations.

unity gain buffer separates the two transducers emulating the propagation in a lossless linear medium, provided with a perfect acoustic reflector, without taking into account for diffraction. The RX CMUT converts the incident force, F , to an electrical signal sensed by the RX amplifier. The three alternatives shown in Fig. 2.1.1 are evaluated: an open-loop voltage amplifier (VA), a resistive-feedback amplifier (RFA) featuring a trans-resistance gain R_f and a capacitive-feedback amplifier (CFA) with a trans-impedance gain $(\omega C_f)^{-1}$. A broadband transconductor, the simplest low-power active stage in CMOS technology, is assumed as active stage for the three amplifiers. C_p in Fig. 2.1.1 represents the parasitic capacitance loading the transducer, due for example to the interconnection between the cells to the amplifier and the input impedance of the transconductor.

Fig. 2.1.2 compares the normalized pulse-echo responses (i.e. the transfer functions from the driving voltage to the output of the RX amplifiers) assuming the components listed in Table 1.3.1 for the CMUT equivalent circuits and $C_p=10$ pF. The VA and CFA feature the same

by the fact that the TX voltage-to-pressure response is band-pass and the purpose of the analysis is to compare the pulse-echo frequency response with different RX configurations, for a fixed TX pressure.

shape of the pulse-echo frequency response with only a negligible difference in the center frequency and bandwidth. On the contrary, the RFA displays a remarkably different frequency response. To gain further insights, closed form equations for the transfer functions are derived. By inspection of the circuit in Fig. 2.1.1, the incident acoustic force on the RX CMUT is:

$$(2.1.1) \quad F = sV_{in}R_m n C_m H(s, \omega_n, Q)$$

with

$$(2.1.2) \quad H(s, \omega_n, Q) = \frac{\omega_n^2}{s^2 + s\frac{\omega_n}{Q} + \omega_n^2}$$

where ω_n and Q are determined only by the mechanical properties of the CMUT:

$$(2.1.3) \quad \omega_n = \frac{1}{\sqrt{C_m L_m}}, \quad Q = \frac{1}{R_m} \sqrt{\frac{L_m}{C_m}}$$

The receive sensitivity, S_{F-V_o} , defined as the gain from F to V_o , i.e. the voltage at the output of the RX amplifiers, depends from the amplifier configuration (the pressure to V_o sensitivity can be calculated by multiplying S_{F-V_o} by the area of the transducer). Assuming sufficiently high transconductance (g_m) of the active stage, the RFA and CFA load the RX CMUT with low impedance². As a result, the electrical capacitors C_0 and C_p are shorted and do not affect the receive sensitivities, given

²The amplifiers active stage considered in the analysis is a transconductor. At first order, the input impedance of the RFA and CFA is $1/g_m$, and is independent from the value of R_f or C_f .

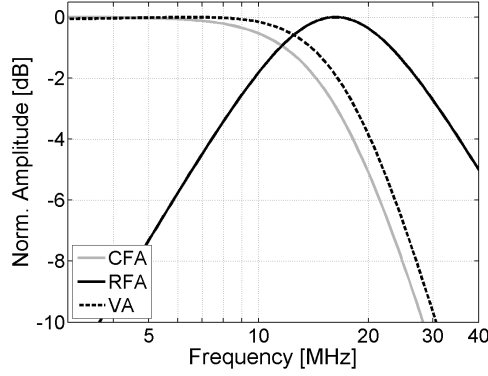


Figure 2.1.3. Simulated RX sensitivities.

by:

$$(2.1.4) \quad S_{F-V_o}|_{RFA} = -sR_f n C_m H(s, \omega_n, Q)$$

$$(2.1.5) \quad S_{F-V_o}|_{CFA} = -\frac{1}{C_f} n C_m H(s, \omega_n, Q)$$

The VA displays high input impedance and provides an output voltage proportional to the voltage drop across the C_0 and C_p :

$$(2.1.6) \quad S_{F-V_o}|_{VA} = A_v \frac{1}{n} \frac{C_m n^2}{C_m n^2 + (C_0 + C_p)} H(s, \omega'_n, Q')$$

where $A_v = g_m R_l$ and $H(s, \omega'_n, Q')$ is given by (2.1.2) by replacing the following expressions for the natural frequency and quality factor:

$$(2.1.7) \quad \omega'_n = \frac{1}{\sqrt{C_{eq} L_m}}, \quad Q' = \frac{1}{R_m} \sqrt{\frac{L_m}{C_{eq}}}$$

with $C_{eq} = \frac{C_m (C_0 + C_p)}{C_m n^2 + (C_0 + C_p)}$

Fig. 2.1.3 plots the RX transfer functions, (2.1.4)-(2.1.6), normalized to the peak gain. The VA and CFA amplifiers display similar low-pass

responses. The gain with the VA configuration is impaired by the parallel combination of C_0 and C_p . In fact, at low frequency the latter form a voltage divider with the equivalent mechanical capacitance reported to the electrical side of the transformer, n^2C_m . The larger is $(C_0 + C_p)$, the lower is S_{F-V_o} , confirmed by (2.1.6). The natural frequency and quality factor of the VA transfer function, given by (2.1.7), are dependent on $(C_0 + C_p)$ through C_{eq} . Nonetheless the impact is mild because n^2C_m is typically quite smaller than C_0 alone (~ 3.3 times for the transducer considered in this work) leading to $\omega'_n \sim \omega_n$ and $Q' \sim Q$.

Differently from the CFA and VA, the RFA yields a band-pass transfer function showing a sensitivity peak at the CMUT natural frequency and the same center frequency of the pulse-echo response. The reason can be physically explained as in [32]. The output voltage of the RFA is proportional to the current flowing through the right-side winding of the transformer in the CMUT equivalent circuit, and the latter is proportional to the current in the mechanical branch. If the CMUT is connected to the CFA or VA, its output current is integrated by the feedback capacitor C_f or by the capacitance $(C_0 + C_p)$ respectively. At frequencies close to the CMUT resonance, given by eq. (2.1.3), the mechanical impedance of the CMUT is dominated by the mechanical loss and the radiation resistance. Therefore, the L_m - C_m - R_m series in the equivalent circuit of Fig.1.3.2 can be approximated with R_m only, and the current, representing the velocity of the membrane, is proportional to the incident force (or pressure). At frequencies lower than the CMUT resonance, the mechanical impedance of the CMUT is dominated by the plate compliance C_m , and the current is proportional to the derivative of the incident force (or pressure).

As a result, if the transducer is operated around the natural frequency ω_n , the RFA provides an output voltage V_o proportional to the incident acoustic force (or pressure). On the other hand, if the transducer is operated below the natural frequency ($\omega < \omega_n$), the CFA and VA provide an output voltage V_o approximately proportional to the incident acoustic force (or pressure), while the output voltage of the RFA is proportional to its derivative, evinced from the zero at the origin in eq. (2.1.4).

In any case, the RFA provides a bandpass RX transfer function with a sensitivity peak at the natural frequency and a shape similar to the TX transfer function, while the CFA and VA low-pass frequency shape RX transfer functions are responsible for the low-frequency shift of the corresponding pulse-echo transfer functions in Fig. 2.1.2.

Multiplying (2.1.1) by (2.1.4)-(2.1.6), the center frequency of the pulse-echo frequency responses are derived with straightforward calculations:

$$(2.1.8) \quad f_0|_{RFA} = \frac{\omega_n}{2\pi}, \quad f_0|_{CFA} \approx f_0|_{VA} = \frac{\omega_n}{2\pi} k_f$$

where $k_f = \sqrt{(2Q^2 - 1 + \sqrt{16Q^4 - 4Q^2 + 1})} / 6Q^2$ increases with Q until saturation to ~ 1 for $Q > 2$. For the CMUT considered in this work $Q=0.713$, yielding $k_f=0.76$. The pulse-echo center frequency with the RFA is 16.2 MHz while with the CFA or VA it is 12.3 MHz.

2.2. Noise Analysis

Noise comparison of different amplifiers can be carried out by evaluating the equivalent input noise. However, with amplifiers having different center frequency and transfer functions, estimation of the equivalent

input noise requires calculation of integrals not yielding closed-form expressions. To circumvent the issue, noise performance of the three RX amplifiers are evaluated by comparing the output noise, with components sized to yield the same sensitivity (gain). Closed form equations for the output noise power spectral densities (PSDs) are derived. Being the output noise PSDs flat, and the same gain assumed for the three amplifiers, the conclusions of the analysis are that same that would have been achieved looking at the equivalent input noise.

The amplifiers noise sources are shown in Fig. 2.1.1. $i_n^2 = 4kT\gamma g_m$ is the noise of the transconductors (being k the Boltzmann's constant, T the absolute temperature and γ a proportionality constant) while $v_n^2 = 4kTR_{l,f}$ is the noise of R_l or R_f in the VA and RFA respectively. To simplify calculations, the transducer equivalent circuit can be approximated as a resistor R_m/n^2 (i.e. the mechanical resistance scaled down by the transformer turn ratio) in parallel with C_0 [18, 41]. The approximation, valid at ω_n , holds over a relatively wide frequency range with broadband transducers because of the low Q. Moreover, since the reactance of $C_0 + C_p$ at ω_n is typically much lower than R_m/n^2 (~ 0.5 k Ω vs 5 k Ω in our case), for output noise calculations the source impedance of the RX amplifiers is further approximated with only C_0 and C_p in parallel. In this condition, the output noise power spectral densities, derived from circuit analysis, are:

$$(2.2.1) \quad V_{n,out}^2|_{CFA} \approx \frac{4kT\gamma}{g_m} \left(\frac{C_0 + C_p}{C_f} \right)^2$$

$$(2.2.2) \quad V_{n,out}^2|_{VA} = 4kT\gamma g_m R_l^2 + 4kTR_l$$

$$(2.2.3) \quad V_{n,out}^2|_{RFA} \approx \frac{16\pi^2 kT\gamma}{g_m} f^2 R_f^2 (C_0 + C_p)^2 + 4kTR_f$$

the three conditions $g_m / (C_0 + C_p) \gg \omega_n$, $R_f (C_0 + C_p) \gg 1/\omega_n$, $C_f \ll (C_0 + C_p)$ are assumed to simplify (2.2.1) and (2.2.3)³. Eq. (2.2.1) and (2.2.2) reveal a flat PSD for the CFA and VA while the first term in (2.2.3), representing the noise PSD contributed by the transconductor in the RFA, is frequency dependent. For noise comparison, we consider an equivalent PSD, calculated by averaging (2.2.3) over $[f_{min} - f_{max}]$, the -3dB bandwidth of the RFA frequency response:

$$(2.2.4) \quad \overline{V_{n,out}^2|_{RFA}} = \frac{\int_{f_{min}}^{f_{max}} V_{n,out}^2|_{RFA}}{f_{max} - f_{min}} \\ = \frac{4kT\gamma}{g_m} R_f^2 (C_0 + C_p)^2 \omega_n^2 \left(\frac{3Q^2 + 1}{3Q^2} \right) + 4kT R_f$$

If, making use of (2.1.4)-(2.1.6), C_f , R_l and R_f are selected to have the amplifiers with the same receive sensitivity, S_{F-V_o} , at the center frequency of the corresponding pulse-echo response (ω_n for the RFA and $k_f\omega_n$ for the VA and CFA), (2.2.1) - (2.2.3) can be rewritten:

³The conditions are commonly satisfied if the CFA and RFA are designed to achieve sufficient gain and a bandwidth larger than the transducer bandwidth.

$$(2.2.5) \quad V_{n,out}^2|_{CFA} \approx \frac{4kT\gamma}{g_m} \left(\frac{C_0 + C_p}{C_m n} \right)^2 \frac{S_{F-V_o}^2}{|H(s = jk_f\omega_n)|^2}$$

$$(2.2.6) \quad V_{n,out}^2|_{VA} \approx \underbrace{V_{n,out}^2|_{CFA}}_{g_m \text{ noise}} + \underbrace{\frac{4kT}{g_m} S_{F-V_o} \frac{C_0 + C_p}{C_m n} \frac{1}{QG(Q)}}_{R_l \text{ noise}}$$

$$(2.2.7) \quad \overline{V_{n,out}^2|_{RFA}} \approx \underbrace{V_{n,out}^2|_{CFA} D(Q)}_{g_m \text{ noise}} + \underbrace{4kT \frac{S_{F-V_o}}{C_m n Q \omega_n}}_{R_f \text{ noise}}$$

$$\begin{aligned} \text{with } G(Q) &= \frac{|H(s = jk_f\omega_n)|}{Q} \\ &= \left(\sqrt{Q^2 k_f^4 - 2Q^2 k_f^2 + Q^2 + k_f^2} \right)^{-1} \end{aligned}$$

$$\text{and } D(Q) = G(Q)^2 \left(\frac{3Q^2 + 1}{3Q^2} \right) \approx \left(\frac{1}{(1.50Q - 0.23)^2} + 1 \right).$$

For a given g_m , (2.2.5)-(2.2.7) demonstrate that the CFA configuration yields the best noise performance. g_m contributes almost to the same noise in the CFA and VA but the latter suffers from additional noise introduced by the load resistor. From (2.2.7), g_m noise in the RFA is the same of the CFA multiplied by $D(Q)$. The latter is a monotonic decreasing function of Q ranging from 5.25 for $Q=0.5$ to ~ 1 for $Q>2$. Hence, g_m noise contribution in the RFA is larger than in the CFA and VA, especially for low- Q broadband transducers. With the CMUT adopted in this work, featuring $Q=0.713$, $D(Q)=2.46$. Also the feedback resistor in the RFA generates output noise but, for designs

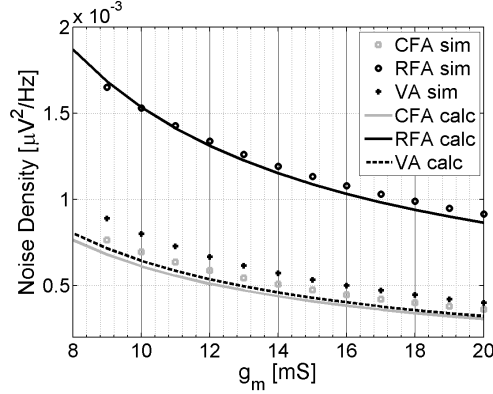


Figure 2.2.1. Simulated and calculated RX amplifiers output noise power spectral density.

aimed at minimizing power consumption, with g_m set close to the minimum to satisfy amplifier bandwidth requirements, the contribution of R_f noise is negligible compared to g_m noise⁴.

Noise generated by the transducer has not been considered in the analysis. It can be represented by a voltage source in series with R_m in the RX CMUT of Fig. 2.1.1 [42]. Since it experiences the same transfer function of the impinging force, if the amplifiers are designed to have the same receive sensitivity the contribution to the output noise is the same in the three cases.

In all the configurations, minimizing C_p , i.e. the parasitic capacitance loading the CMUT, is crucial to limit noise. Moreover, noise can be reduced by selecting higher g_m , at the expense of larger power dissipation, as long as the amplifiers noise is dominant over the transducer contribution.

To gain further insights and prove the validity of the analysis, the simulated output noise for the three amplifiers at different g_m is shown

⁴Looking at eq.(2.2.4), the noise of the transconductor is inversely proportional to g_m , while R_f noise is independent from g_m . Power dissipation of the amplifier is set by the g_m . Therefore, in a low power design, g_m noise is the most important contribution. On the opposite, in a design targeting low noise, with a high transconductance gain active stage, R_f noise may become dominant over g_m noise.

in Fig. 2.2.1 and compared against (2.2.5)-(2.2.7). The amplifiers have been designed to achieve a peak sensitivity $S_{F-V_o}=200$ V/N, requiring $R_f = 12.15$ k Ω and $C_f = 1$ pF in the RFA and CFA respectively. The RX transfer functions, normalized to the peak gain, are reported in Fig. 2.1.3. The g_m noise proportionality constant is $\gamma=1$. Despite the approximations introduced in the analysis, simulations and calculations are in good agreement. Notably the RFA, which is the most widely adopted CMUT amplifier, has the worst noise performance. At $g_m=10$ mS its simulated output noise voltage PSD is 1.5×10^{-15} V²/Hz, ~ 2.2 times larger than with the CFA, mostly due to higher contribution from the transconductor noise (noise of R_f is only 0.2×10^{-15} V²/Hz). The CFA and VA have very similar noise performance, being the impact of R_l noise in the VA negligible. These two amplifiers are therefore preferable to achieve low noise at minimum power consumption. However, it is worth to remember, by comparing (2.1.5) and (2.1.6), that the VA gain is sensitive to C_p while the CFA is not. C_p absorbs also the parasitic coupling capacitance between adjacent transducers and the VA is expected to provide low immunity to crosstalk between nearby transducers, responsible for image quality degradation. The CFA is therefore preferable in view of integration of dense CMUT arrays. Moreover, the feedback architecture of the CFA suppresses the distortion introduced by the transconductor leading to higher dynamic range.

It is also worth remembering that the RFA provides a bandpass RX transfer function and, consequently, a pulse-echo frequency response centered at the CMUT natural frequency, yielding increased sensitivity at higher frequencies as compared to VA and CFA. Therefore, as far as high-frequency applications are foreseen, RFA is likely to be preferred.

CHAPTER 3

A Transceiver Front-End Design

Fig. 3.0.1 shows the block diagram of the CMUT transceiver front-end. The design leverages the BCD8-SOI technology from STMicroelectronics, an evolution of the BCD technology with junction isolations replaced by SiO_2 dielectric. It offers three thin and one thick metal layers, high-voltage devices, and low-voltage, high-speed $0.18\mu\text{m}$ and $0.35\mu\text{m}$ CMOS transistors withstanding 1.8V and 3.3V maximum voltage swing respectively. High voltage devices, adopted in the design, are DMOS (either N- and P-channel) with $1\mu\text{m}$ minimum gate length supporting maximum V_{GS} and V_{DS} of 3.3V and 100V respectively. The SOI isolation limits parasitic capacitances improving speed and power dissipation. Moreover, in view of integration of many transceivers on the same chip, the better isolation performance of SOI, compared to PN junctions, enables a much more compact layout and significant area saving.

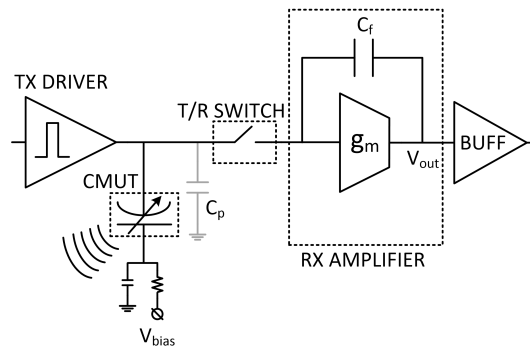


Figure 3.0.1. Block diagram of the CMUT transceiver front-end.

The transceiver front-end comprises a high-voltage TX driver, a T/R switch and a low-noise RX amplifier, followed by buffer for measurement purposes. The transceiver is connected to the individual electrode of the CMUT array element, while an R-C network is used to apply the bias voltage to the common electrode of the CMUT array. If a positive biasing DC voltage is applied to the common electrode, the resulting voltage across the CMUT during TX is less or equal to the absolute value of the bias voltage, thus preventing the CMUT itself from collapsing. Such approach makes it possible to maximize the CMUT receive sensitivity by applying a bias voltage close to the collapse voltage. Detailed descriptions of the design and optimization of the building blocks are provided in the following subsections.

3.1. RX amplifier

The RX amplifier in Fig. 3.0.1 is realized with a transconductor and the feedback capacitor C_f . From eq. (2.1.5), the gain from the impinging force to the output voltage is set solely by transducer parameters and C_f . Given the transducer capacitance and the parasitic capacitance C_p , the transconductance of the active stage, g_m , sets the bandwidth and noise performance and its selection determines the power consumption. The estimated value of C_p is ~ 10 pF. The relatively large value is because the CMUT is interfaced to the front-end through a PCB connector. By leveraging advanced packaging or 3D integration to place the CMUT in closer proximity to the front-end, C_p is expected to reduce drastically, leading to a substantial performance improvement.

Approximating the source impedance of the amplifier with a capacitor of value $C_0 + C_p$, and assuming negligible capacitance loading the

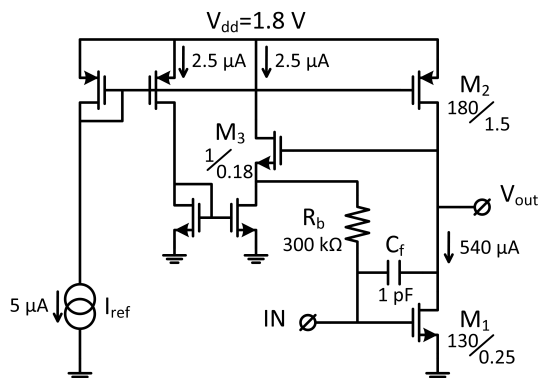


Figure 3.1.1. Schematic of the RX amplifier.

amplifier output node, the -3dB amplifier bandwidth is given by:

$$(3.1.1) \quad BW \approx \frac{g_m}{C_0 + C_p}$$

As a rule of thumb, a minimum constrain for the g_m can be found imposing the amplifier bandwidth to be at least twice the resonance frequency of the transducer, $g_m > 2\omega_n (C_0 + C_p) = 3.9$ mS.

According to eq. (2.2.5) in Section II and the plot shown in Fig. 2.2.1, the higher g_m and the lower is the amplifier noise. We target a noise contribution from the amplifier comparable to the noise of the transducer and the estimated g_m is 10 mS, larger than what required to satisfy the -3dB bandwidth constraint. The feedback capacitance is set to 1 pF, providing a receive sensitivity of 232 V/N.

The schematic of the amplifier is shown in Fig. 3.1.1. Power dissipation is set to 1 mW, corresponding to 550 μ A from the 1.8 V supply. Transistor M_1 , sized for $g_m=10$ mS, determines the transconductance of the stage. M_2 sets the bias current to M_1 , by mirroring I_{ref} . The level shifter M_3 and resistor R_b are used for biasing the gate of M_1 . Compared to a simple resistor, the use of a level shifter sets the output quiescent voltage to $V_{gs1} + V_{gs3}$ (≈ 550 mV + 400 mV), close to $V_{dd}/2$,

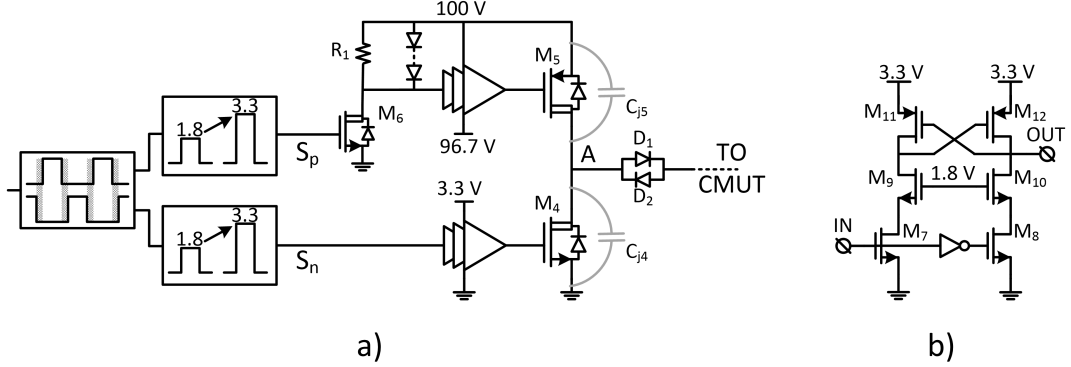


Figure 3.1.2. Schematic of the TX driver (a) and low-voltage level shifter (b).

maximizing 1dB compression point and hence the amplifier dynamic range. The level shifter is biased at low current density by the nMOS current mirror. R_b introduces a zero at DC and a pole at frequency $1/(2\pi C_f R_b)$ in the transfer function and a large value has been selected to push the pole at sufficiently low frequency (≈ 530 kHz). The size of M_1 has been selected to achieve the desired transconductance with a non-minimum channel length to limit the in-band $1/f$ noise contribution.

3.2. TX Driver

The high-voltage TX driver is shown in Fig. 3.1.2(a). Transistors M_4 - M_5 provide unipolar pulses of 100 V across the CMUT electrodes during transmission. Device aspect ratios are $1600\mu\text{m}/1\mu\text{m}$ and $4100\mu\text{m}/1\mu\text{m}$. Large size is selected to achieve rise and fall time of ≈ 15 ns, suited for an excitation frequency of 10 MHz. The reverse biased drain-to-bulk junctions, represented by the diodes in the DMOS symbols, load node-A with a large parasitic capacitance, $C_{j4} + C_{j5} \approx 5$ pF. Diodes D_1 - D_2 are used to disconnect the CMUT from node-A during reception, when M_4 and M_5 are off. In this case the CMUT is loaded

approximately by the parasitic capacitance of $D_1 - D_2$ of 90 fF only, much lower than $C_{j4} + C_{j5}$, thus preventing a significant SNR penalty.

The TX driver is controlled by 1.8V input pulse trains. To prevent simultaneous conduction of the output stage devices (M_4 - M_5), complementary signals are first provided with a conventional non-overlapping clock generation circuit, implemented with thin-oxide 0.18 μ m gates. High-voltage transistors occupy large area and, in order to minimize their size (set by the required on-state resistance) they must be driven with the maximum allowed overdrive voltage. Therefore, the 0-1.8V pulse trains at the output of the non-overlapping clock generator are translated to 0-to-3.3V control signals (S_p , S_n) with the latch-based level shifter shown in Fig. 3.1.2(b). It consists of a cross-coupled pair (M_{11} - M_{12}) driven by the input transistors (M_7 - M_8), allowing fast commutation with zero static power dissipation. M_9 - M_{12} are 0.35 μ m transistors, able to sustain the 3.3V output swing while M_7 - M_8 are thin-oxide devices protected from the large output voltage by M_9 - M_{10} .

S_p has to be further translated to a voltage ranging from 96.7 V to 100 V. Different techniques have been reported in literature to realize high voltage shifters. A latch-based architecture, similar to the topology in Fig. 3.1.2(b) is proposed in [15]. The drawback is the need for six high-voltage transistors, occupying large area. A more compact solution is adopted in [43] where the level shifter is realized with a simple common-source stage loaded with a diode-connected device. The main issue of this approach is the slowness in the turn-off transition, due to the limited discharging current capability of a diode-connected transistor. Moreover, the active load requires large overdrive

to achieve high-voltage swing, mandating selection of high current (and hence power dissipation) or small transistor size, penalizing speed.

In this design, the high-voltage level shifter is realized by M_6 and R_1 in Fig. 3.1.2(a). The approach is similar to [43] but the diode-connected load is replaced by R_1 , mitigating the above issues and requiring less silicon. The maximum voltage drop on R_1 is limited to 3.3 V by a battery of diodes, ensuring robustness against components spread due to process variations. The high-voltage shifter draws current when M_6 is on. To limit power dissipation, the gate of the high-voltage pMOS M_5 is driven by a tapered buffer chain, scaling the load capacitance of the high-voltage MOS down to 18 fF from 6 pF. An identical buffer chain drives M_4 to match the delays experienced by S_p and S_n . Size of M_6 is $6\mu\text{m}/1\mu\text{m}$ and $R_1=6.4\text{ k}\Omega$. The simulated contribution to power dissipation of the level shifters and driving circuits is less than 10% of the high-voltage output stage.

3.3. T/R Switch

The schematic of the T/R switch is shown in Fig. 3.3.1. DMOS M_{13} withstands the high-voltage TX pulses. It must provide high off-state isolation to protect the sensitive RX amplifier and at the same time low on-resistance to limit SNR and bandwidth degradation. To gain insight, considering its channel resistor r_{on} in series to the CFA input, the following expressions for bandwidth and output noise can be derived:

$$(3.3.1) \quad BW \approx \frac{1}{(C_0 + C_p) \left(r_{on} + \frac{1}{g_m} \right)}$$

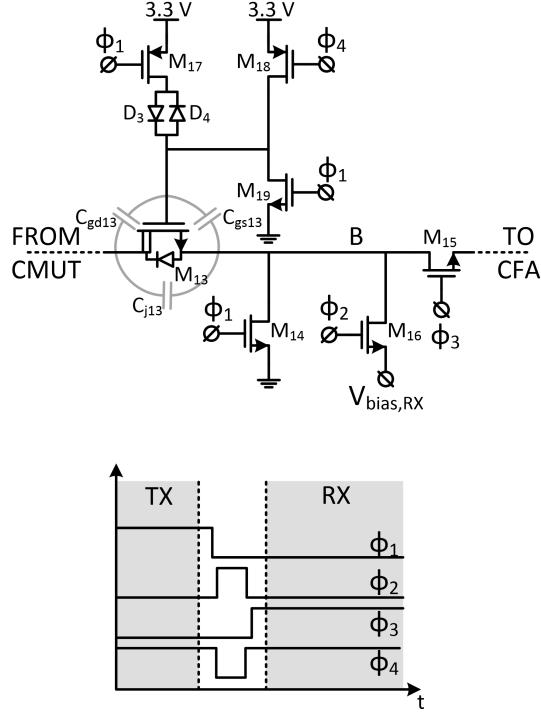


Figure 3.3.1. Schematic of the T/R switch (top) and timing of the control signals (bottom).

$$(3.3.2) \quad N_{out}^2 \approx 4kT \left(r_{on} + \frac{\gamma}{g_m} \right) \left(\frac{C_0 + C_p}{C_f} \right)^2$$

Thus, not to compromise too much the amplifier performance, r_{on} must be comparable or lower than $1/g_m$. On the other hand, low r_{on} trades with transistor size, leading to large device parasitic capacitances and area occupation. We selected $W_{M_{13}} \approx 100 \mu\text{m}$, leading to $r_{on} \approx 100 \Omega$ and $C_{par} \approx 1 \text{ pF}$. Diodes $D_3 - D_4$, connected to the 3.3 V supply by M_{17} , are introduced to decrease the equivalent parasitic capacitance in RX mode to approximately 120 fF. M_{19} keeps the gate of M_{13} well-biased to ground in off-state while M_{18} avoids the diodes voltage drop by bootstrapping the gate control signal when M_{13} is switched on.

A further drawback of choosing a too large width for M_{13} is the penalty in the off-state isolation due to signal leakage through the large parasitic junction capacitance of the drain to bulk diode, C_{j13} in Fig. 3.3.1. Most of the previously reported T/R switches [10, 14, 15, 18] are realized with a single high-voltage device in series to the RX amplifier input. The off-state isolation, i.e. the voltage attenuation from the input to the output of the T/R switch, is only 20 dB in our case. Being 100 V the maximum pulser output voltage, the attenuation provided by a single device is not enough to ensure protection of the RX amplifier. To solve this issue transistor M_{14} shunts node-B to ground when M_{13} is off while M_{15} , driven by Φ_3 , disconnects the input of the RX amplifier in order to not perturb the DC biasing point. Finally M_{16} , driven by Φ_2 , is introduced to speed-up the time required to switch from TX to RX mode by pre-charging the top plate of the CMUT to $V_{bias,RX} = V_{GS,M_1}$ (being V_{GS,M_1} the gate-to-source voltage of M_1 in Fig. 3.1.1). With this solution, the simulated settling time to switch between transmission to reception is reduced to 4 μ s. Without M_{16} the top plate of the CMUT would have to be charged by the RX amplifier with an excessively long time constant. $V_{bias,RX}$ is a low impedance biasing voltage, generated with a replica of the core transistors in the RX transconductor, that can be shared among several transducers. M_{14} , M_{15} , M_{16} are low-voltage, high-speed transistors introducing negligible parasitic capacitances due to the small dimensions.

3.4. Experimental Results

A microphotograph of the realized integrated circuit is shown in Fig. 3.4.1. The active die area, excluding the output buffer introduced for measurement purposes, is approximately 0.18 mm². Prototypes of

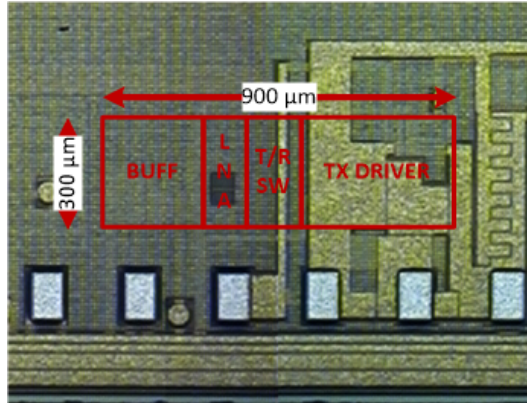


Figure 3.4.1. Chip photograph.

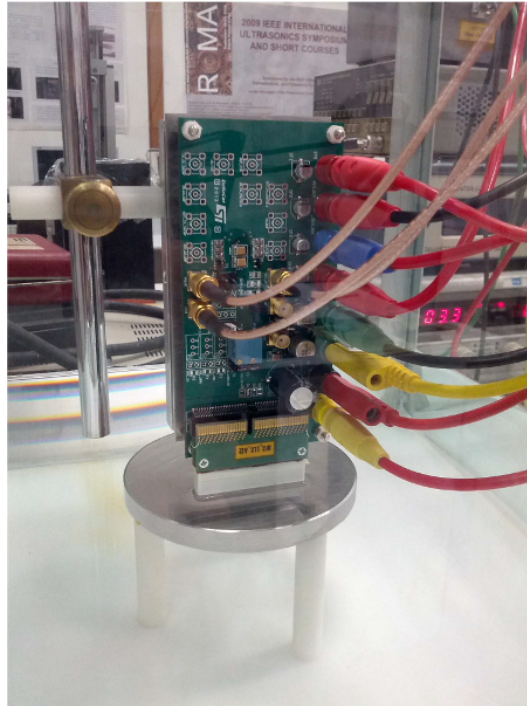


Figure 3.4.2. Test board with the CMUT probe head immersed in a water tank.

the transceiver are bonded directly on a custom designed PCB, which also mounts the connector for the CMUT probe head. Fig. 3.4.2 shows a photograph of the test board with the transducer immersed in a water tank. The high voltage required to bias the common electrode of the

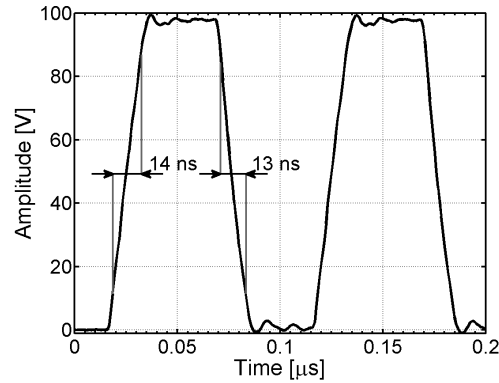


Figure 3.4.3. Measured TX pulses at 100V supply.

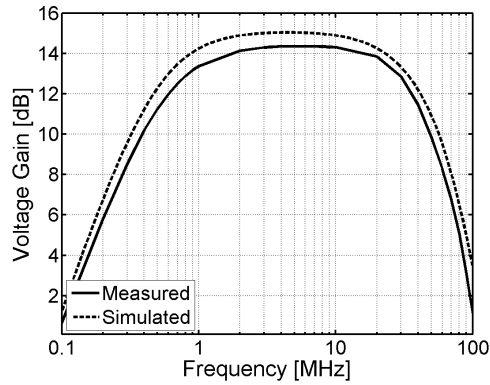


Figure 3.4.4. Measured and simulated RX voltage gain.

CMUT array (see the block diagram in Fig. 3.0.1) is generated with discrete components.

Measured pulses at 10MHz frequency, delivered by the TX driver with 100V supply are shown in Fig. 3.4.3. The rise and fall time from 10% to 90% of the peak-to-peak voltage are 14 ns and 13 ns respectively.

Fig. 3.4.4 compares the measured and simulated voltage gain of the RX path. In this case, a 10pF capacitor in series with a voltage source replaces the transducer. Measurements and simulations are in good agreement. The peak gain is 14.2 dB, with -3dB bandwidth extending

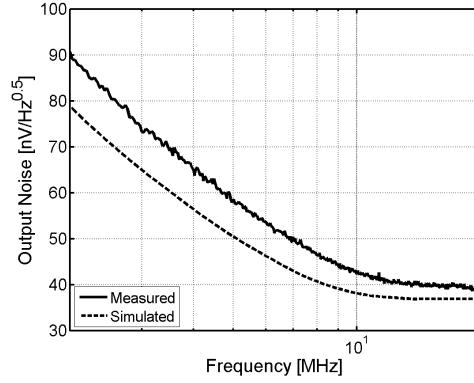


Figure 3.4.5. Measured and simulated RX output noise.

from 500 kHz to 40 MHz. The output voltage at 1dB gain compression, determined through large signal measurements with a sinusoidal excitation, is of 564 mV_{0-pk} .

The measured and simulated output noise spectral density is shown in Fig. 3.4.5. The $1/f$ noise corner is $\sim 4\text{MHz}$. The Noise Figure, calculated by normalizing the total noise to the estimated contribution of the transducer, is 8.9 dB.

An extensive electro-acoustic characterization has been carried out. For pulse-echo measurements, the probe head was immersed in a water tank, facing a stainless steel planar reflector placed at the elevation focal distance of 1.5 cm. The TX drives the CMUT with pulse trains and the reflected echoes are recorded after switching to RX mode. Fig. 3.4.6(a) shows the received signals with a CMUT bias voltage ranging from 150 V to 270 V. The normalized pulse-echo frequency responses, corresponding to the FFT of the received time-domain signals when the transmitter delivers very short isolated pulses of $\sim 20 \text{ ns}$ (in order to excite the entire CMUT frequency band) are reported in Fig. 3.4.6(b). As expected, bandwidth and center frequency are slightly affected by the CMUT bias voltage due to the spring softening effect [29]. At the

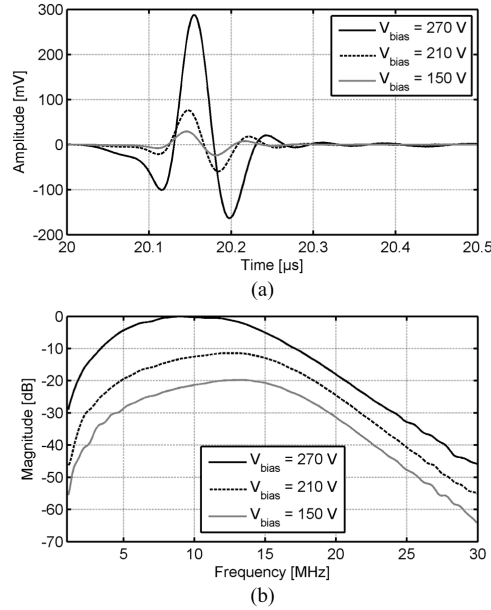


Figure 3.4.6. Received echoes (a) and pulse-echo frequency response (b) for different values of the bias voltage, from 150 V to 270 V.

maximum value of 270 V, center frequency is 10 MHz and the -6dB bandwidth is $\sim 100\%$, extending from 4.4 MHz to 15.4 MHz.

The receive sensitivity has been estimated by processing two different measurement sets. The plot in Fig. 3.4.7(a) shows the transmitted pressure frequency response, measured with a needle type MHA9-150 hydrophone (Force Technology, Brøndby, Denmark) placed at twice the elevation focal distance of the probe. In this circumstance, it can be assumed that the incident pressure on the hydrophone is the same received by CMUT during the pulse-echo measurements. The receive sensitivity frequency response is then computed by dividing the spectra of the pulse-echo by the transmit sensitivity. The resulting curves, reported in Fig. 3.4.7(b) display a low-pass shape, as expected from the

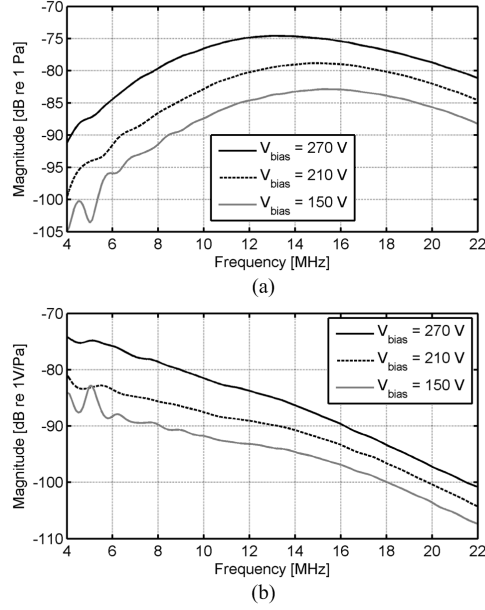


Figure 3.4.7. Transmit pressure(a) and receive sensitivity (b) for different values of the bias voltage, from 150 V to 270 V.

use of a capacitive-feedback amplifier. However, a quantitative discrepancy between the slope of the experimentally estimated and the simulated frequency responses is observable. This discrepancy is likely due to the fact that the equivalent circuit model used in this paper does not take into account the frequency-dependant acoustic attenuation of the silicone rubber constituting acoustic lens of the CMUT probe. Moreover, the equivalent circuit models the radiation impedance as purely resistive, while the experiments were performed using a limited sized transducer array element, characterized by a lateral dimension of the order of a wavelength, whose radiation impedance is characterized by a not negligible reactive part, mainly inductive, representing the mass loading of the propagation medium.

With 270V CMUT bias voltage, the receive sensitivity at the center frequency of the pulse-echo response, 10 MHz, is 72 mV/kPa.

Table 3.4.1. MEASUREMENT SUMMARY AND COMPARISON

	This Work	[18]	[32]	[9]	[10]	[14]	[8]
CMUT capacitance [pF]	9.2	40	0.15	0.3	1.57	0.23	0.09
k_T^2	0.23	-	-	0.25	-	-	-
Center Frequency [MHz]	10	3	15	2.2	5.1	2.6	20
Bandwidth [MHz]	11	5.2	10	5	6.4	2.6	8.6
Pulse Amplitude [V]	100	30	-	25	25	15	25
RX Sensitivity [mV/kPa]	72	162	130	414	70	-	-
Input Noise [$\text{mPa}/\sqrt{\text{Hz}}$]	0.55	0.56	3	0.9	1.8	-	-
Noise Figure [dB]	8.9	10.3	1.8	-	-	-	-
Dynamic Range [dB]	70	60	42	-	-	-	50
RX Amp. Power [mW]	1	14.3	6.6	2.4	4	0.328	0.8
RX Amp. FoM [$\text{mPa}\sqrt{\text{mW}/\text{Hz}}$]	0.55	2.1	7.7	1.4	3.6	-	-

The output noise, integrated over the pulse-echo bandwidth, is $133 \mu\text{V}_{\text{rms}}$, corresponding to an equivalent noise spectral density superimposed to the incident pressure of $N_{\text{in}} = 0.55 \text{ mPa}/\sqrt{\text{Hz}}$. The estimated input pressure at 1dB gain compression is 7.83 kPa and the dynamic range of the receiver, defined by the ratio of the maximum signal at 1dB compression to the minimum signal at SNR=0 dB, is 70 dB.

Furthermore, the transmit pressure generated with the maximum TX pulse amplitude was measured by placing the hydrophone at 2 mm from the transducer surface. The CMUT biased at 270 V was driven with a 100V, 10-cycle burst at 10 MHz. The peak-to-peak amplitude of the pressure signal recorded, shown in Fig. 3.4.8, is approximately 500 kPa. The difference in the positive and negative peak amplitudes observable is due to the CMUT nonlinear large-signal response.

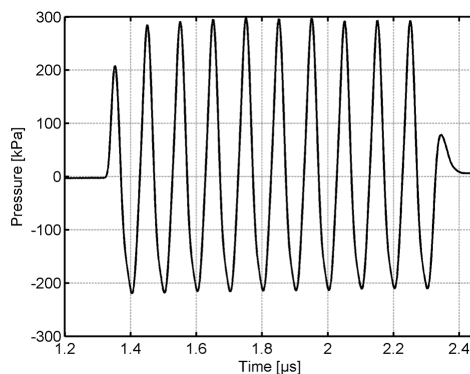


Figure 3.4.8. Acoustic pressure measured at 2 mm from the CMUT biased at 270 V and excited with a 100V, 10-cycle burst at 10 MHz.

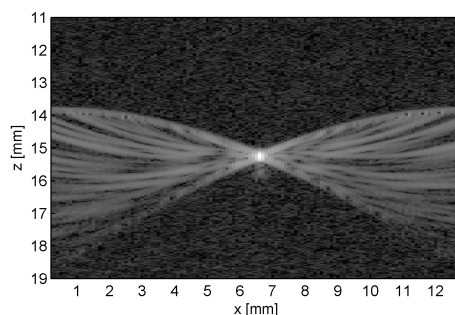


Figure 3.4.9. SAF image of a copper wire immersed in water obtained by mechanically scanning the CMUT with a 100 μ m step. Each scan line is obtained by beamforming 128 signals. The dynamic range of the image is 80 dB.

Measured electro-acoustic results demonstrate performance comparable to a commercial probe based on piezoelectric transducers operating in the same frequency range [1].

Finally, an ultrasound image of a 40 μ m-diameter copper wire immersed in water was obtained by mechanically scanning the CMUT and by acquiring the pulse-echo signal at each position. The CMUT was driven in the same conditions of the TX pressure measurements, using a 2-cycle burst at 10 MHz. The 256 rf signals resulting from

a 25.6cm scan using a 100 μ m step were filtered, using a tapered cosine window with -3dB cut-off frequencies of 4.4 MHz and 15.6 MHz, and beamformed with a single-element Synthetic Aperture Focusing (SAF) algorithm using 128-element apertures to form each scan line. The obtained image, normalized to the maximum signal amplitude and log-compressed, is represented in Fig. 3.4.9 using a very high dynamic range of 80 dB, in order to make visible both point spread function sidelobes and background noise. The SNR was computed, using the uncompressed rf beamformed data, as the ratio between the rms amplitude of the point target signal S_{rms} and of the noise N_{rms} estimated in a dark portion of the image, resulting in a value of $SNR_m = 20\log_{10}\left(\frac{S_{rms}}{N_{rms}}\right) = 66.7$ dB. In order to assess the measured SNR performance, the expected SNR for a 128-element SAF aperture, assuming uncorrelated additive noise for the receiver and neglecting the signal loss due to the array element directivity, was computed from the receiver dynamic range (70 dB), compensated for the ratio between the maximum output voltage of the receiver (564 mV) and the maximum signal amplitude of the acquired rf data (167 mV), resulting in the value of $SNR_e = 10\log_{10}(128) + 70 - 20\log_{10}\left(\frac{V_{max-o}}{V_{max-rf}}\right) = 80.5$ dB. The 14dB discrepancy between the measured and predicted SNR is partially attributed to the simplifying analytical assumption that the peak signal amplitude is constant for all the scan lines (while acquisitions with the transducer far from the center experience up to 8dB loss) and correlated noise on the supply voltages, not sufficiently filtered out in the experimental setup. Nevertheless, the high excitation voltage of the TX driver, paired with the low noise and high linearity of the RX amplifier, enable excellent image SNR and dynamic range.

The performance of the front-end are summarized and compared against previously reported CMUT front-ends in Table-3.4.1. Sufficient information to estimate the transducer electromechanical conversion factor are provided only in [9], yielding $k_T^2=0.25$, similar to our case. Compared to previous works, the proposed transceiver shows the highest TX pulse amplitude and RX dynamic range. The equivalent input noise is the lowest, similar to [18] but with more than 10x power saving. A Figure of Merit, (FoM) has been recently introduced in [18] to compare the performance of CMUT RX amplifiers. As discussed in [18], the $FoM = \frac{P_{n,rms-in}}{\sqrt{BW}} \sqrt{P_{diss}}$ normalizes the equivalent rms input noise pressure ($P_{n,rms-in}$) to power dissipation and bandwidth (P_{diss} and BW). At first order, the transducer area does not change the FoM. For the VA, the area of the transducer does not affect both the receive sensitivity (eq. 2.1.6) and generated noise (eq. 2.2.2). For the CFA or RFA, neglecting C_p , a larger CMUT area improves the pressure receive sensitivity but, due to a larger equivalent capacitance C_0 , it rises the noise generated by the core amplifier by the same amount (see eq. 2.2.1,2.2.3). The FoM allows a fair comparison of amplifiers designed for transducers of different size and operating frequency. FoM does not account for the area of the RX amplifier. However, the latter is not a limiting factor being the area of the transceiver typically dominated by TX high-voltage devices. The proposed front-end demonstrates the best FoM of $0.55 \text{ mPa}\sqrt{\text{mW/Hz}}$. This has been achieved by identifying the optimal amplifier configuration and through careful circuit design to minimize the amplifier noise generation.

CHAPTER 4

CMUT Second Harmonic Compensation

In previous chapters, the CMUT has been considered as a linear transducer whose equivalent model is represented in Fig. 1.3.2. In reality, high-voltage driven CMUTs [31] behave nonlinearly due to the nonlinear relationship between the applied voltage and the generated electrostatic force. This characteristic is a strong drawback with respect to piezoelectric transducers that are much more linear. The linearity of PZT is exploited in the so called “nonlinear ultrasound imaging” or “second harmonic imaging”. Nonlinearity of human tissue distorts the ultrasonic wave during propagation, this causes higher harmonics. The second harmonic is read back to produce better image quality. For this reason linear behavior of ultrasonic transducers is a stringent requirement in nonlinear ultrasound imaging.

CMUT electrostatic nonlinearity was previously investigated [44], and its dynamic non-instantaneous characteristic was validated. Since then, several linearization approaches were proposed. In the first studies [45,46], open-loop linearization methods based on a “trial and error” pre-distortion of the driving signal were proposed. Successively [47] a more rigorous formalization of the problem was proposed and a closed-loop driving method called “gap-feedback” was theorized. Practical implementation requires large capacitors and/or inductors so applications are limited. In successive studies [48,49] improved techniques produced better performance, but practical bounds limit well-designed

implementation. In general, any open-loop linearization approach utilizes predistorted analog excitation signals with a spectral content to compensate the harmonic distortion introduced by CMUTs. In order for the pre-distortion to be successfully applied to the driving signal, knowledge of the input-output CMUT nonlinear characteristic is necessary [50]. This kind of method requires the use of high-voltage linear transmitters limiting practical implementation to high-end imaging systems. In this chapter we investigate the use of an open-loop linearization approach applied to digital unipolar excitation pulses where the pre-distortion is achieved by acting on the amplitude (A), duty cycle (D), and slope of the rising (Sr) and falling (Sf) edges of the pulses. A high-voltage unipolar pulser topology capable of generating trapezoidal shaped signals is designed. This circuit is suitable for integration in existing silicon process technology. An integrated circuit (IC) prototype with digital control capability of the trapezoidal signal wave-shape was fabricated and interconnected the CMUT probe head. Transmit pressure measurements with the CMUT in immersion operation were performed.

4.1. Linearization Technique

The electrostatic force $F_e(t)$ acting on the two electrodes depends squarely on the instantaneous charge, which is proportional to the applied voltage $V(t)$ divided by the instantaneous gap $g(t)$:

$$(4.1.1) \quad F_e = -\frac{\epsilon_0 A}{2} \left(\frac{V(t)}{g(t)} \right)^2$$

where A is the electrode area. Rearranging the expression, the following equation is obtained:

$$(4.1.2) \quad V(t) = g(t) \sqrt{\frac{2}{\varepsilon_0 A} F_e(t)}$$

that can be rewritten as a function of the gap normalized to the zero-bias gap (g_n), and the electrostatic force normalized to the biasing electrostatic force (F_n):

$$(4.1.3) \quad V(t) = g_n(t) \frac{V_{bias}}{g_{bn}} \sqrt{F_n(t)}$$

Eq. 4.1.3 can be used for the implementation of an open-loop charge control strategy by defining the desired electrostatic force signal $F_n(t)$, and by predicting the gap behavior $g_n(t)$.

In collaboration with the University Roma 3, we developed a software using Matlab (MathWorks Natick, MA) to synthesize unipolar predistorted analog waveforms to be applied to the CMUT designed to suppress second harmonic emission. Then we approximate the synthesized analog waveform with a trapezoidal waveform to be realized with an efficient integrated circuit. To get the right trapezoidal waveform, we derive the frequency spectrum of the desired analog waveform. Then we derive the analytical expression of the spectrum of a trapezoidal pulse with the same center frequency as a function of the aforementioned parameters A , D , S_r , and S_f . We successively find the values of the trapezoidal pulse parameters by equating the two spectra at the fundamental and second-harmonic frequencies. Fig. 4.1.1 shows one period of a 100V, 7MHz pre-distorted analog waveform and the corresponding pre-distorted digital pulse computed using the developed algorithm.

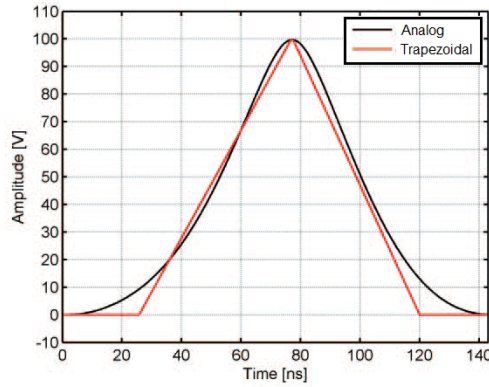


Figure 4.1.1. 100V, 7MHz analog and trapezoidal pre-distorted waveforms.

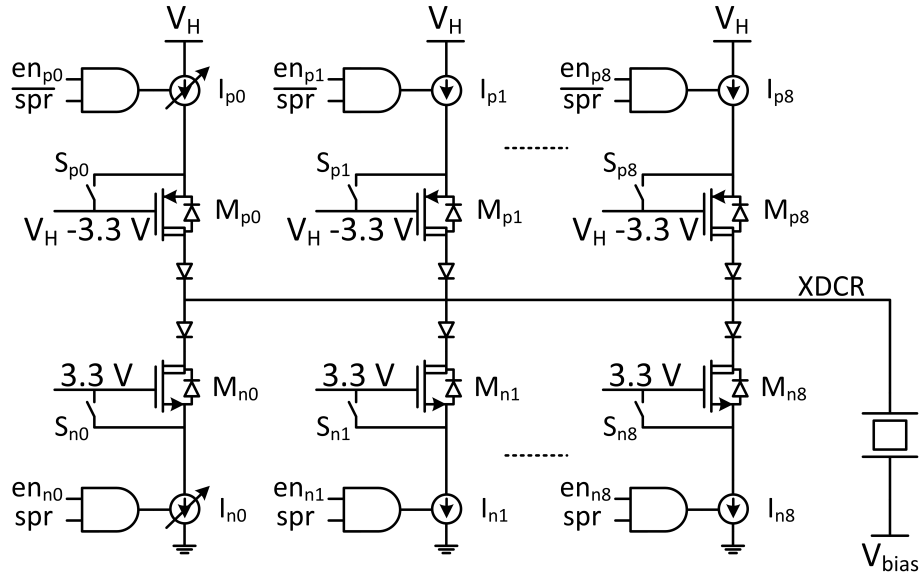


Figure 4.2.1. Simplified schematic of the high-voltage tunable pulser.

4.2. High-Voltage Tunable Pulser

Fig. 4.2.1 shows the simplified block diagram of the proposed high-voltage driver. It provides tunable trapezoidal pulses across the CMUT electrodes ranging from 0 to V_H , with a maximum amplitude of 200 V. To obtain a finite slope of the output signal rising and falling edges, the electrical capacitance of the CMUT is charged and discharged at constant current. The charging current is selectable with en_{p0-8} that

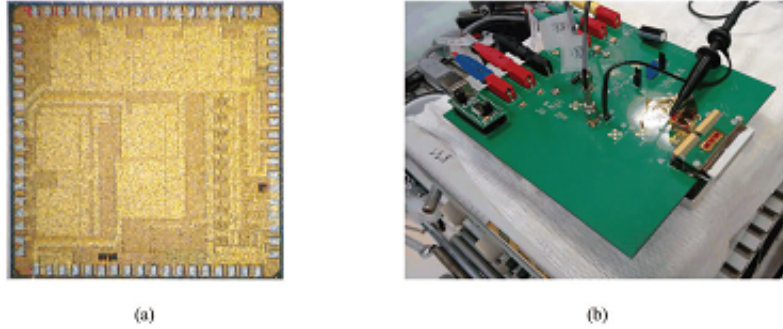


Figure 4.2.2. Pulser IC (a) and test PCB (b). The test PCB hosts the connectors for the CMUT probe-head and for the IC digital control signals and power supply.

enable the current generators I_{p0-8} . Conversely, the discharging current is selected with en_{n0-1} to enable I_{n0-8} . Each parallel branch generates a constant current of 20 mA when enabled. I_{n0} and I_{p0} are digitally programmable current generators from 2.5 mA to 20 mA. These current generators are obtained with low-voltage MOS, while high-voltage DMOS M_{n0-8} and M_{p0-8} are added to sustain the high-voltage swing of the output node. Switches S_{n0-8} and S_{p0-8} are used to turn off the single branches, when necessary. Finally, spr is a square-wave burst signal generated from the digital core of the IC. It provides the timing for the driver with a coarse duty cycle selection of 10 ns (given from the 100 MHz system clock). Auxiliary analog circuits provide a fine duty cycle selection with ≈ 100 ps resolution. The proposed circuit was fabricated using a BCD-SOI technology by STMicroelectronics (Milan, Italy). The fabricated test chip [Fig. 4.2.2(a)] was wire bonded to a PCB [Fig. 4.2.2(b)] containing connectors for auxiliary signals, power supplies and few external components. The PCB was provided with a connector for the insertion of the CMUT probe-head. The probe-head used was a 10MHz, 192-element linear array, with 0.2 mm pitch and no elevation focus, having a single-element capacitance of 23 pF and a

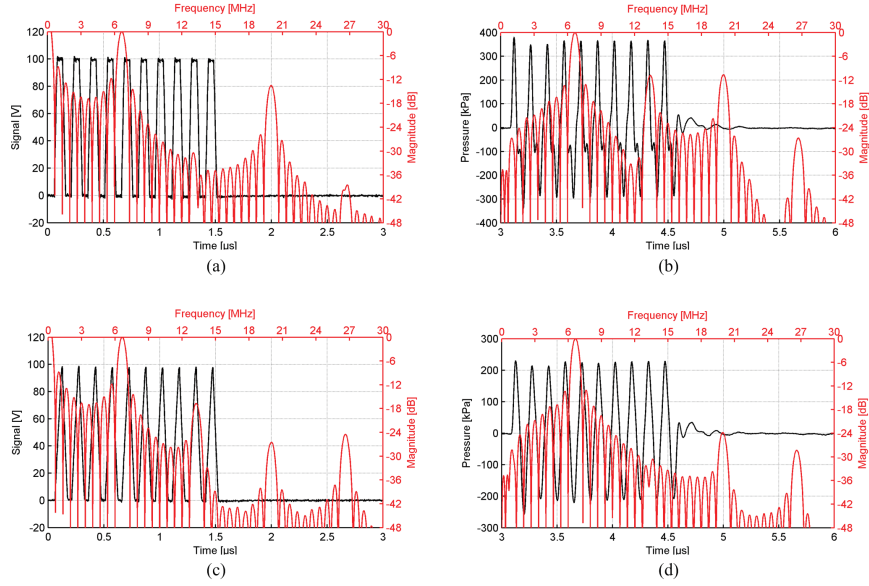


Figure 4.3.1. Excitation pulse trains [square (a) and trapezoidal (c)] and pressure signals [(b) and (d) respectively] measured at 4.5 mm from the CMUT surface.

collapse voltage of 270 V. The pulser output is connected to one of the individual electrodes of the CMUT array, while an R-C bias is used to apply the bias voltage (V_{bias} in Fig. 4.2.1) to the common electrode of the CMUT array.

4.3. Experimental Results

We performed transmit pressure measurements in a water-tank setup. A needle type MHA9-150 hydrophone (Force Technology, Brøndby, Denmark) was placed in front of the water-immersed CMUT at a distance of 4.5 mm. The CMUT was biased at $\sim 90\%$ of the collapse voltage (240 V). We made a first measurement by exciting the CMUT with a 100V square unipolar 10-cycle pulse train at 7 MHz. Fig. 4.3.1(a) shows the signal measured at the output of the pulser and its computed spectrum. The second harmonic level generated by the pulser itself was

less than 30 dB below the fundamental. Fig. 4.3.1(b) shows the pressure signal generated by the CMUT, characterized by a harmonic-to-fundamental ratio (HFR) of -11 dB. We then generated a 100V trapezoidal 10-cycle pulse train at 7 MHz by programming the pulser using the parameters achieved with the pre-distortion algorithm, fed with a set of electrical impedance measurements performed on the CMUT at different bias voltages in the 140-240V range. Fig 4.3.1(c) shows the generated trapezoidal signal and its spectrum, while Fig 4.3.1(d) reports the pressure signal generated by the CMUT, showing a HFR of less than -30 dB.

CHAPTER 5

PGA Design for Time-Gain Compensation

In Section 1.1, we described the basic physical principles governing the ultrasound wave propagation. In particular, equation 1.1.6 shows the exponential attenuation to which the wave is subject. As a rule of thumb, the pressure attenuation in the human body is $1 \frac{dB}{MHz \cdot cm}$. The frequencies used for imaging are application dependent and ranges from 1 MHz to >20 MHz. As an example with an 8-MHz probe and 4-cm depth penetration and accounting for both outgoing and return attenuation, the signal amplitude variation from the internal tissues will attenuate by 64 dB (or $4cm \times 8MHz \times 1 \frac{dB}{MHz \cdot cm} \times 2$) from reflections near the surface. In order to achieve 50 dB of imaging resolution and accounting for losses due to bone, instrument cables, and other mismatches, the desired dynamic range approaches 119 dB. To put this into perspective, a $0.3V_{pp}$ full-scale signal with a $10nV/\sqrt{Hz}$ noise floor in a 50MHz bandwidth implies a 63dB input dynamic range. Additional dynamic range is achieved by using multiple channels (RX beam forming) which increases the dynamic range by a factor of $10 \log(N_{ch})$. This implies that thousands of channels have to be integrated together to achieve the desired dynamic range. This poses a strict limit to the power dissipation of each RX channel - not only to the RX amplifier but also to the analog to digital converter (ADC) at the end of the channel. Fortunately, the ADC specifications can be relaxed since the entire

dynamic range is not needed at all instants of time. By taking into account that the propagation attenuation is proportional to the distance, and that the distance is proportional to the elapsed time (considering constant speed of sound), an ADC with less than full dynamic range can be used by sweeping the gain of the amplifier to match the attenuation of the received reflection over time (proportional to depth of penetration). This is called time-gain compensation (TGC).

To realize a perfect time-gain compensation, a Programmable- Gain Amplifier (PGA) with dB-linear gain control is needed (i.e. a linear change of the control signal results in an exponential gain change). This involves the implementation of an exponential function, challenging to achieve with the square-law and linear I-V characteristics of MOS devices. In addition, wide range of gain variation, large bandwidth, and rail-to-rail output swing with low power consumption are commonly required features [51–53]. To simultaneously achieve all the aforementioned specifications we investigated the performance of the cross-coupled pair for discrete-time linear amplification and we show that its regeneration feature proves to be attractive for implementing Programmable-Gain Amplifiers (PGA).

5.1. PGAs: Requirements and Limitations

Both programmable and variable gain amplifier (PGA/VGA) are fundamental analog building blocks used in a wide variety of systems such as medical equipment, disk drives, wireless communication, hearing aids, and so on. VGAs are tuned continuously by analog control signals, whereas PGAs are tuned discretely by digital control signals. The main function of a PGA/VGA is to provide a fixed output power from a wide variation in the input signal amplitude in order to maximize

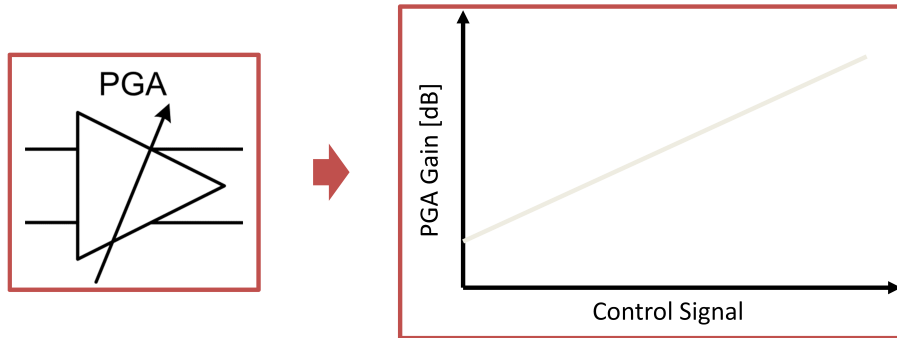


Figure 5.1.1. PGA linear-in-dB gain control.

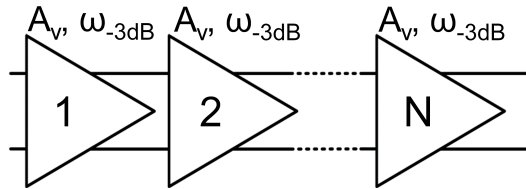


Figure 5.1.2. Multistage amplifier block diagram.

the dynamic range of the entire system. Design specifications can vary significantly depending on the application. Large voltage-gain range, low power, low noise, wide bandwidth, and high large-signal linearity are common requirements for these circuits. They are typically employed in an automatic gain control (AGC) loop. In order to maintain uniform loop transient response and settling time, and to prevent a resolution problem of the control signal, the dB-linear gain characteristic shown in Fig. 5.1.1 is required for the PGA/VGA. The latter involves the implementation of an exponential function which is challenging to obtain in CMOS technology due to the linear and square characteristic of the MOSFET itself.

The common solution adopted for state-of-the-art PGA design is an open-loop multi-stage approach as shown in Fig. 5.1.2. Cascading identical stages improves the gain-bandwidth product. Each stage has a limited gain variation range that simplifies the dB-linear gain control,

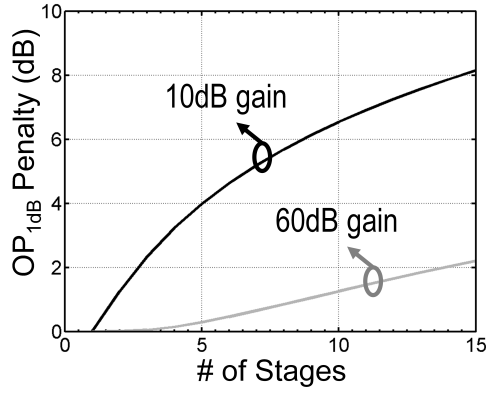


Figure 5.1.3. Output 1dB compression point of the chain as a function of the number of stages.

however the multi-stage approach has an intrinsic linearity disadvantage. In particular, the 1dB compression point at the output of the Nth stage (OP_{1dB_N}) is a function of the output 1dB compression point of each stage (OP_{1dB_1}):

$$(5.1.1) \quad OP_{1dB_N} \approx \left(A_v^{N-1} \sqrt{\left| \frac{A_v^2 - 1}{A_v^{2N} - 1} \right|} \right) OP_{1dB_1}$$

where A_v is the gain of the single stage and N is the number of stages. From this equation, we can see that there is always a penalty represented by the term in brackets. Fig. 5.1.3 shows the linearity penalty as a function of the number of stages. For high gain the penalty is low (i.e. 2dB with 15 stages at 60dB gain). For low gain, when the input signal is maximum and highest linearity is needed, the penalty is significant (i.e. 8dB with 15 stages at 10dB gain). To overcome this limitation we found an alternative approach achieving higher GBW performance in a single stage, and subsequently better linearity.

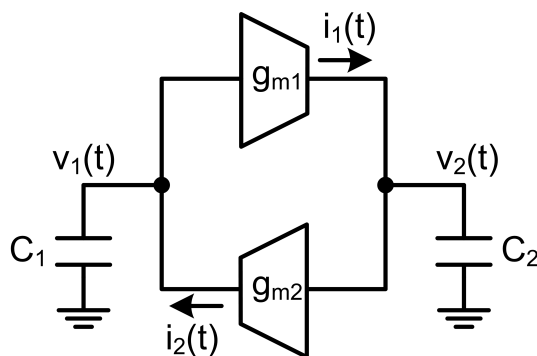


Figure 5.2.1. Cross-coupled pair block diagram.

5.2. Cross-Coupled Pair Regeneration: Theory

Cross-coupled pairs (XCPs) are among the most widely adopted fundamental circuits in use today. This elegant device arrangement yields broadband positive feedback with high gain and low power. Both features are desirable in analog and digital applications [54–56]. Its small signal properties are consistently leveraged in oscillators, impedance negators and to boost gain of transconductors. The bistable behavior is exploited in static latches and memory cells, and the regeneration capability is leveraged in the design of sense amplifiers and high-speed comparators.

The XCP could be modeled as shown in Fig. 5.2.1. It is composed of two transconductors (g_{m1} and g_{m2}) and two load capacitors (C_1 and C_2). g_{m1} drives g_{m2} and vice versa, leading to a positive feedback with one metastable state ($v_1 = v_2 = 0$). If the circuit is imbalanced from its metastable state, then the two output voltages tend to diverge in different direction. This behavior can be described with the following

equations:

$$(5.2.1) \quad \begin{cases} \frac{dv_1(t)}{dt} C_1 &= -g_{m2} v_2(t) \\ \frac{dv_2(t)}{dt} C_2 &= -g_{m1} v_1(t) \end{cases}$$

which can be solved applying the Laplace transformation

$$(5.2.2) \quad \begin{cases} (sV_1 + v_{10}) C_1 &= -g_{m2} V_2 \\ (sV_2 + v_{20}) C_2 &= -g_{m1} V_1 \end{cases}$$

where $v_{10} = v_1(t = 0)$ and $v_{20} = v_2(t = 0)$ are the initial conditions.

With straightforward calculations, considering $g_{m1} = g_{m2} = g_m$ and $C_1 = C_2 = C_l$, it is possible to find the differential-mode ($V_{dm}(t)$) and common-mode ($V_{cm}(t)$) evolution:

$$(5.2.3) \quad \begin{cases} V_{dm}(t) = V_2(t) - V_1(t) &= v_{dm0} A_{dm} = (v_{20} - v_{10}) e^{\frac{g_m}{C_l} t} \\ V_{cm}(t) = \frac{V_2(t) + V_1(t)}{2} &= v_{cm0} A_{cm} = \left(\frac{v_{20} + v_{10}}{2} \right) e^{-\frac{g_m}{C_l} t} \end{cases}$$

where v_{dm0} and v_{cm0} are the initial condition for the differential-mode and the common-mode voltages. A_{dm} and A_{cm} are the differential and common-mode gains. Interestingly the common-mode voltage decreases exponentially with the increasing time whereas the differential-mode voltage is exponentially amplified. Therefore, if an initial differential voltage is applied across the load capacitors, the XCP regenerates the voltage with an exponential rate. This suggests that the XCP could be exploited to build an amplifier. As an example, Fig. 5.2.2 shows the proposed amplification phases, where V_{out} represents the differential-mode of the XCP. The circuit is used in three phases of operation. First of all the circuit is reset and the load capacitors are pre-charged to the metastable state. Then during the sampling phase, the outputs

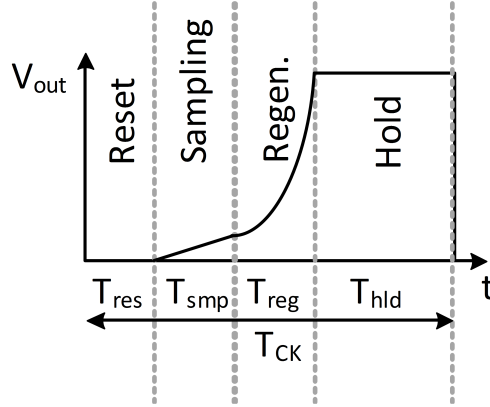


Figure 5.2.2. Amplification phases.

are imbalanced to a value proportional to the amplifier input signal. The regeneration takes place in the third phase, during which the XCP is enabled and the output rises exponentially following the eq. (5.2.3). A last fourth phase is optional where the XCP is disabled and the capacitors hold the final output voltage for ADC conversion.

5.2.1. Noise Analysis. Common frequency domain noise analysis assumes that the amplifier is in steady state, but this is not the case for the XCP whose amplification is based on the natural response of the system. Therefore the usual assumption of wide-sense-stationary (WSS) noise sources is not valid. To analyze the noise performance of the XCP it is necessary to make use of nonstationary noise analysis as is described in [57]. This method uses time domain analysis to find the nonstationary noise at the desired node. Because the variance of the output noise is a function of time, the results are more realistic than frequency domain analysis.

Fig. 5.2.3 shows the equivalent half-circuit model of the XCP used to perform the noise analysis. S_{res} is the switch performing the reset, C_l is the load capacitor, g_m is the transconductor closed in a positive loop and $I_n = 4kT\gamma g_m$ is the equivalent white noise source. At $t=0$, the

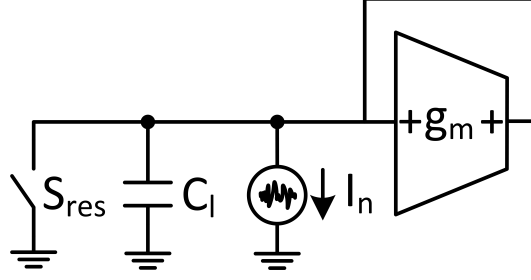


Figure 5.2.3. XCP equivalent half circuit for noise analysis

reset switch is opened and the noise on the capacitor can be calculated as

$$(5.2.4) \quad v_n^2 = \frac{1}{2} I_n \int_0^t |h_n(t)|^2 dt$$

where $h_n(t)$ is the impulse response from the noise current source to the voltage at the node of interest. From circuit inspection the g_m connected as in Fig. 5.2.3 is equivalent to a negative resistor of value $-1/g_m$. The output can be shown to be

$$(5.2.5) \quad h_n(t) = \frac{1}{C_l} e^{\frac{g_m}{C_l} t} u(t)$$

where $u(t)$ is the unit step function. With straightforward calculations:

$$(5.2.6) \quad v_n^2 = \frac{\gamma kT}{C_l} e^{2\frac{g_m}{C_l} t}$$

Dividing this by the squared differential gain $A_{dm}^2 = e^{2\frac{g_m}{C_l} t}$ and simplifying $\gamma \approx 1$, it turns out that the equivalent input noise of the half circuit is given by the well known kT/C_l . Interestingly, this is independent from g_m . This demonstrate that increasing the power consumption on the XCP does not provide any noise advantage.

The noise coming from the reset phase has to be added to this term. It's contribution is well known in literature and it is equal to

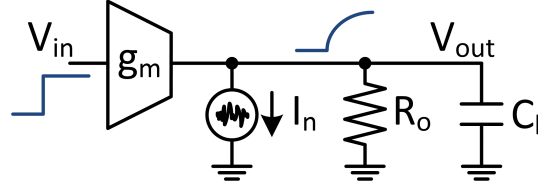


Figure 5.2.4. Preamplifier equivalent model.

kT/C_l . Finally, taking into account the differential realization of the XCP, all the calculated noise terms have to be doubled so the total input noise of the periodically reset (clocked) XCP is $4kT/C_l$. The only way to decrease the noise is by increasing C_l or by amplifying the signal during the sampling phase with a preamplifier.

Fig. 5.2.4 shows a simple preamplifier easily implemented in CMOS technology. It models as a transconductor g_m with a resistive load R_o and a capacitive load C_l . As before, $I_n = 4kT\gamma g_m$ is the equivalent white noise source. In this application, the preamplifier is clocked as well (i.e. it is enabled only during the sampling phase for a small amount of time (T_{smp})). Therefore it can be analyzed as a nonstationary circuit with the aforementioned method. The output noise can be calculated applying 5.2.4

$$(5.2.7) \quad n_{out}^2(t) = \frac{\gamma kT}{C_l} g_m R_o \left(1 - e^{-\frac{2t}{\tau}} \right)$$

with $\tau = R_o C_l$. To find the equivalent input noise, the output noise has to be divided by the squared time-dependent gain

$$(5.2.8) \quad G(t) = \frac{v_{out}(t)}{v_{in}(t)} = g_m R_o \left(1 - e^{-\frac{t}{\tau}} \right)$$

leading to

$$(5.2.9) \quad n_{in}^2 = \frac{\gamma k T}{g_m} \frac{1}{\tau} \frac{\left(-1 - e^{-\frac{t}{\tau}}\right)}{\left(-1 + e^{-\frac{t}{\tau}}\right)}$$

from which it is possible to gain a useful design insight. For given time t (e.g. sampling time T_{smp} fixed by the application) and capacitance C_l (e.g. chosen for XCP requirements), the input noise decreases when R_o increases. To gain further insights, two cases can be identified:

- $T_{smp} \gg \tau$: the circuit behaves as a voltage amplifier (VA)

$$G = g_m R_o; n_{out}^2 \approx (\gamma k T / C_l) g_m R_o \text{ thus}$$

$$(5.2.10) \quad n_{in}^2|_{VA} \approx \frac{\gamma k T}{g_m} \frac{1}{\tau}$$

- $T_{smp} \ll \tau$: the circuit behaves as an integrator (INT) $G =$

$$(g_m / C_l) T_{smp}; n_{out}^2 \approx (\gamma^2 k^2 T g_m / C_l^2) T_{smp} \text{ thus}$$

$$(5.2.11) \quad n_{in}^2|_{INT} \approx \frac{\gamma k T}{g_m} \frac{2}{T_{smp}}$$

Considering that in our application the T_{smp} is fixed, the time constant of a voltage amplifier should be at least $\tau = T_{smp}/5$ (in order to have enough time for the output to settle). This leads to

$$(5.2.12) \quad n_{in}^2|_{VA} \approx \frac{\gamma k T}{g_m} \frac{5}{t_{smp}} > n_{in}^2|_{INT}$$

In terms of noise, the integrator has a clear advantage over the voltage amplifier. For all applications for which the amplifier is enabled for a fixed amount of time, an integrator leads to less noise than a voltage amplifier.

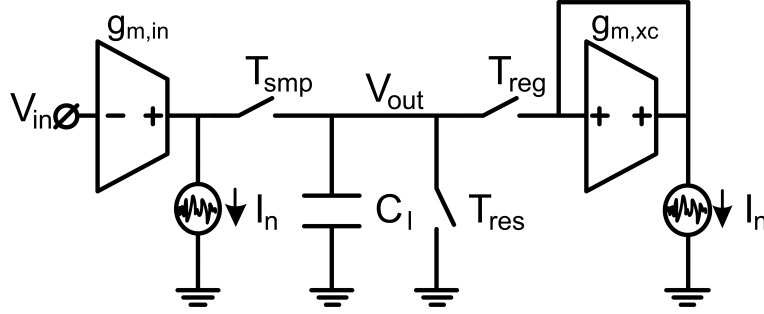


Figure 5.2.5. Block diagram of the proposed amplifier.

Now that we have chosen the preamplifier topology, Fig. 5.2.5 shows the half-circuit representation of the complete amplifier. $g_{m,in}$ represents the preamplifier transconductor while $g_{m,xc}$ represents the transconductor of the XCP. Applying the aforementioned equations, the equivalent input noise for the half circuit is:

$$(5.2.13) \quad n_{in}^2 \approx \underbrace{\frac{2kT\gamma}{g_{m,in}T_{smp}}}_{\text{Preamplifier}} + \underbrace{\frac{kT\gamma}{g_{m,in}^2T_{smp}^2}}_{\text{XCP}} + \underbrace{\frac{kT}{g_{m,in}^2T_{smp}^2}}_{\text{Reset}}$$

and for the differential circuit:

$$(5.2.14) \quad n_{in}^2 \approx \underbrace{\frac{4kT\gamma}{g_{m,in}T_{smp}}}_{\text{Preamplifier}} + \underbrace{\frac{2kT\gamma}{g_{m,in}^2T_{smp}^2}}_{\text{XCP}} + \underbrace{\frac{2kT}{g_{m,in}^2T_{smp}^2}}_{\text{Reset}}$$

The following section will demonstrate that a moderate gain in the sampling phase is sufficient to make the other noise sources negligible, leaving the input transconductors as the primary noise source.

So far, a perfect timing for the sampling phase and the regeneration phase was assumed. In a real implementation the timing circuit will be affected by jitter. Thus it is worth to study the effect of the jitter on the different amplification phases. The most significant effect can be seen in the sampling phase and in the regeneration phase. Let us firstly analyze the sampling phase. In presence of a timing uncertainty, the

gain of the preamplifier (implemented as an integrator) can be written as

$$(5.2.15) \quad G_{smp} = \frac{g_{m,in}}{C_l} (T_{smp} + dt_{smp})$$

where dt_{smp} represents the random deviation of T_{smp} during one amplification cycle. The desired signal is $V_{in} \frac{g_{m,in}}{C_l} T_{smp}$, on which it is superimposed an unwanted component $V_{in} \frac{g_{m,in}}{C_l} dt_{smp}$. Noticing that the unwanted component is signal dependent it follows that a jitter on T_{smp} leads to a limitation of the SNR, expressed as:

$$(5.2.16) \quad SNR_{smp} = \frac{V_{in} \frac{g_{m,in}}{C_l} T_{smp}}{V_{in} \frac{g_{m,in}}{C_l} dt_{smp}} = \frac{T_{smp}}{dt_{smp}} \rightarrow \frac{T_{smp}}{\sigma_{smp}}$$

where σ_{smp} is the rms jitter (standard deviation of the random variable dt_{smp} changing cycle after cycle). Similar considerations apply for the regeneration phase. The gain can be expressed as:

$$(5.2.17) \quad G_{reg} = e^{\frac{g_{m,xc}}{C_l} (T_{reg} + dt_{reg})}$$

since $dt_{reg} \ll T_{reg}$, it can be approximated as:

$$(5.2.18) \quad G_{reg} \approx e^{\frac{g_{m,xc}}{C_l} T_{reg}} \left(1 + \frac{g_{m,xc}}{C_l} dt_{reg} \right)$$

leading to an SNR limit of:

$$(5.2.19) \quad SNR_{reg} \approx \frac{C_l}{g_{m,xc} dt_{reg}} \rightarrow \frac{C_l}{g_{m,xc} \sigma_{reg}}$$

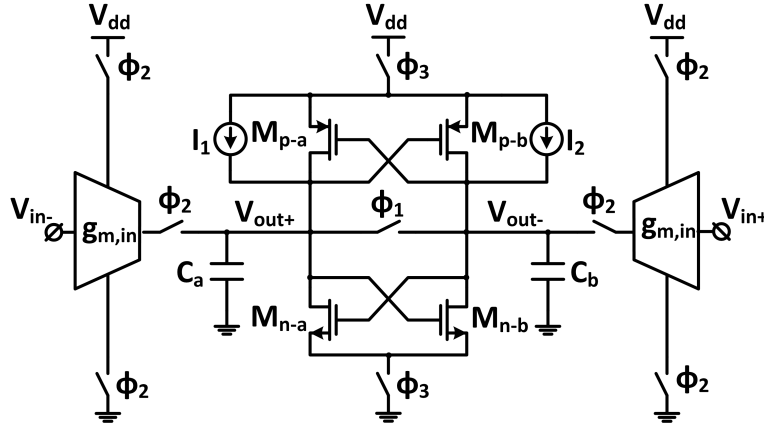


Figure 5.3.1. Schematic of the PGA core.

Eq. (5.2.16) and (5.2.19) suggest that the timing circuit has to be carefully designed to push the SNR limit high enough for the desired application.

5.3. PGA Design Exploiting the XCP Regeneration

By exploiting regenerative amplification, the exponential growth of the output voltage naturally enables a dB-linear gain control. At the same time regeneration greatly outperforms the linear gain-bandwidth (GBW) trade-off of continuous-time amplifiers [58], yielding excellent driving capability at high frequency and with low power. As a proof of concept, test chips of the PGA have been realized in a $0.18\mu\text{m}$ CMOS technology. Measurements demonstrate dB-linear amplification from 15 dB to 66 dB over 50MHz bandwidth with $\approx 0.6\text{dB}$ maximum gain error. While driving 2pF load capacitors, the amplifier achieves a record GBW up to 100 GHz with only $420\mu\text{W}$ power consumption. The core of the PGA is shown in Fig. (5.3.1). It is composed of two complementary cross-coupled pairs ($M_{n-a,b}$, $M_{p-a,b}$) and sampling capacitors ($C_{a,b}$) driven by a pair of transconductors ($g_{m,in}$) realized with CMOS inverters. The circuit is clocked by three phases (Φ_1 , Φ_2 , Φ_3) with tim-

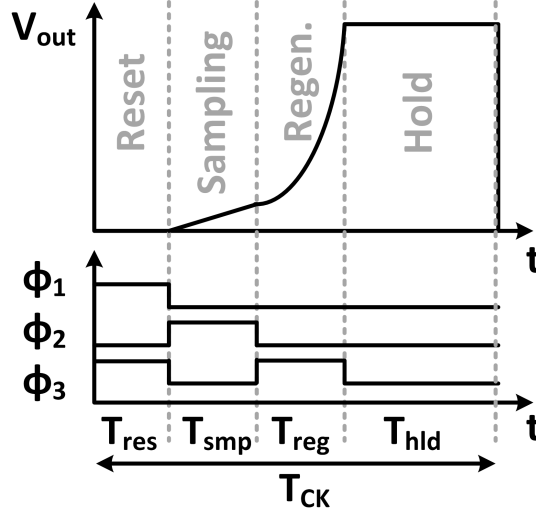


Figure 5.3.2. PGA timing diagram.

ing diagram shown in Fig. (5.3.2) and period T_{ck} . In each period the differential output voltage V_{out} is first zeroed by shorting the two capacitors $C_{a,b}$ and the common-mode voltage set to $\approx V_{dd}/2$ by switching on the cross-coupled pairs with Φ_1 and Φ_3 simultaneously high. In the next phase (Φ_2 high) the input signal is partially amplified and sampled on $C_{a,b}$. If a short sampling time (T_{smp}) is selected, the differential input voltage V_{in} is amplified approximately by $(g_{m,in}/C_{a,b})T_{smp}$ at the end of Φ_2 . Regeneration takes place in the next phase, by supplying the cross-coupled pairs with Φ_3 high: $M_{n-a,b}$ and $M_{p-a,b}$ shunt $C_{a,b}$ with a negative resistance yielding a negative time constant $\tau_{reg} = -C_{a,b}/g_{m,xc}$ (being $g_{m-xc} = (g_{m,n} + g_{m,p})$) and an exponential growth of V_{out} . After regeneration, lasting T_{reg} , the circuit enters the hold mode. With Φ_1 - Φ_3 low, the cross-coupled pairs are switched off and the final value of V_{out} is stored on $C_{a,b}$. The gain experienced by the sampled value of V_{in} is

$$(5.3.1) \quad \frac{g_{m,in}}{C_{a,b}} T_{smp} e^{\frac{T_{reg}}{|\tau_{reg}|}}$$

evidencing an exponential dependence from $T_{reg}/|\tau_{reg}|$. Thus, dB-linear gain control can be easily achieved by changing linearly T_{reg} . Regeneration allows extremely high gain, yielding extraordinarily high GBW. As an example, with $f_{ck}=100$ MHz the signal bandwidth is limited to 50 MHz by the sampled-time operation. With the component selected in the design ($g_{m,xc}=2.5$ mS and $C_{a,b}=2$ pF), $|\tau_{reg}|=800$ ps. Assuming 0dB gain in the sampling phase and maximum T_{reg} limited to $0.5T_{ck}$ (to leave margin for the reset, sampling and hold phases) the resulting gain is 54.3 dB. The corresponding GBW is 25.9 GHz, ~ 130 higher than the GBW of a continuous-time amplifier driving $C_{a,b}$ with the same g_m of the cross-coupled pairs. To prevent saturation at maximum gain, static and dynamic offsets are corrected by the two current sources I_1 and I_2 shown in Fig.(5.3.1), driven differentially by a charge pump.

The input transconductors and the cross-coupled pairs mostly determine noise of the amplifier. Considering thermal noise, the equivalent input noise power, n_{in}^2 , is given by eq. (5.2.14), providing useful design insights. Interestingly, the contribution of the cross-coupled pairs (the second term in eq. (5.2.14)) is independent from $g_{m,n}$ and $g_{m,p}$. Moreover, a moderate gain in the sampling phase is sufficient to make it negligible, leaving the input transconductors as the main noise source. Finally, the equation suggests increasing the sampling time T_{smp} to reduce $v_{n,in}^2$. Because T_{smp} increases also the gain in the sampling phase, the optimal value needs to be chosen as a compromise between noise performance and gain compression of the input transconductors. We selected $g_{m,in}=3.5$ mS and $T_{smp}=2.5$ ns, providing 12.8 dB gain in the sampling phase and $V_{n,in}^2=(54.3 \text{ Vrms})^2$. As depicted in Fig.(5.3.3),

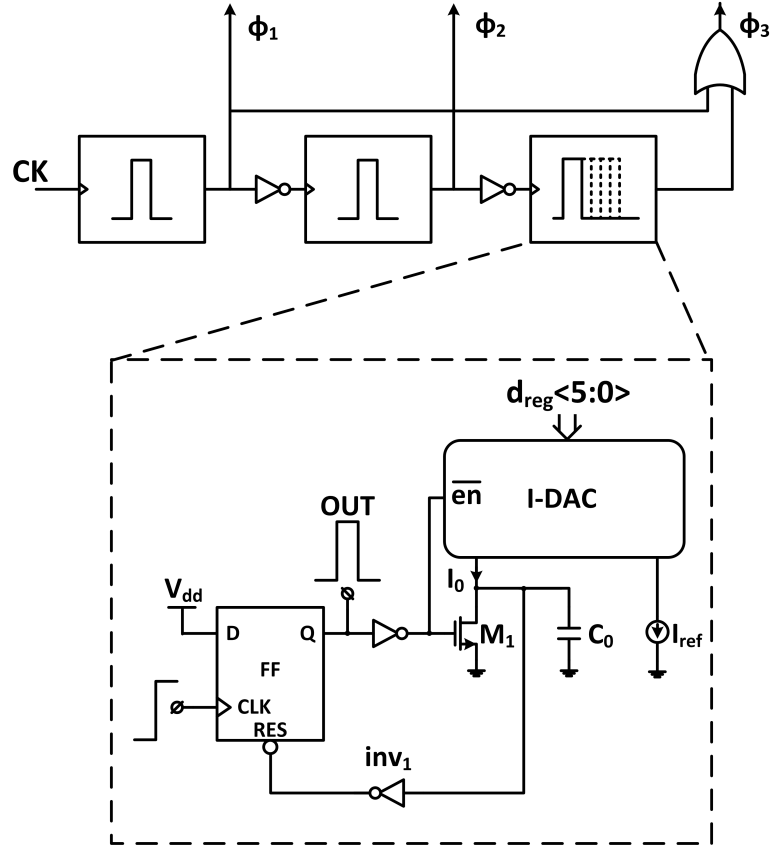


Figure 5.3.3. Cascaded pulse generators.

three cascaded pulse generators, driven by an external clock, provide the amplifier control signals. T_{reg} is made programmable with the circuit shown in the figure. The operation is as follows: the output is normally low and capacitor C_0 shorted to ground by M_1 . A rising edge on the CLK input of the flip-flop triggers the output pulse. The output of the flip-flop goes high enabling C_0 to be charged with the current I_0 . When the voltage across C_0 reaches the logic threshold of inv_1 , the flip-flop is reset and the output goes low. I_0 is set with a 6-bit resolution DAC, allowing a linear control on the output pulse duration. Timing jitter in the control signals limits the amplifier SNR. From circuit analysis, the sampling and regeneration phases, Φ_1 and Φ_3 are the most critical. The corresponding SNR is given by the equations (5.2.16) and

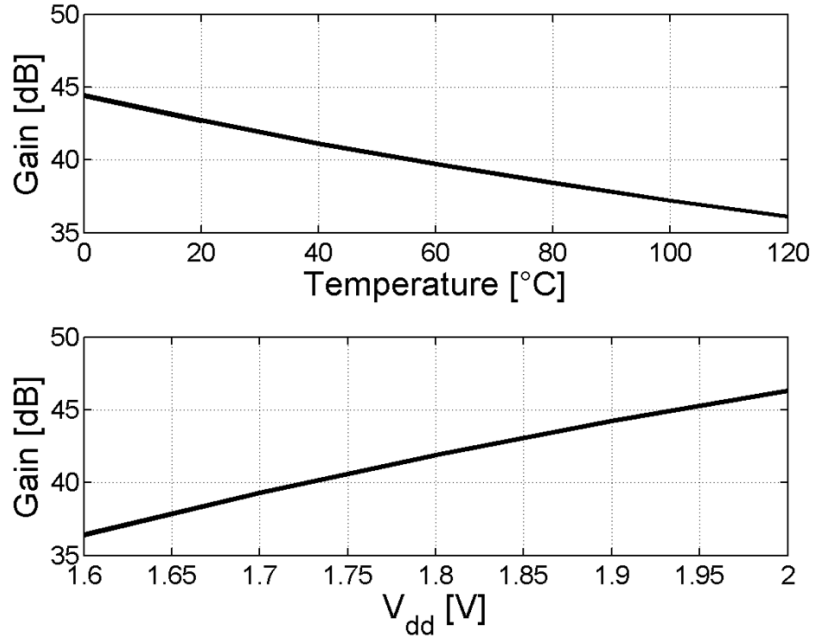


Figure 5.3.4. Gain variation as a function of temperature and supply voltage.

(5.2.19). The pulse-generators are designed to achieve 8ps maximum jitter, leading to $SNR_{smp} \approx 50$ dB and $SNR_{reg} \approx 40$ dB.

Process, supply voltage and temperature (PVT) variations affect the gain of the amplifier. Process variation can be trimmed one-off while voltage and temperature should be continuously compensated with an AGC loop. Nevertheless simulations have been performed to evaluate the effect of VT variations on the designed circuit. Fig. 5.3.4 shows the simulation results when the PGA is programmed to have 40dB gain. The gain variation remains within 8 dB with respect to the temperature variation (from 0°C to 120°C) and 10 dB with respect to the power supply variation (from 1.6 V to 2 V). This range of variation is in-line with that of commonly adopted open-loop circuits and it is expected to be less than that of multi-stage amplifiers. As an example, the amplifier in [52] has 15 continuous-time amplifying stages, each one

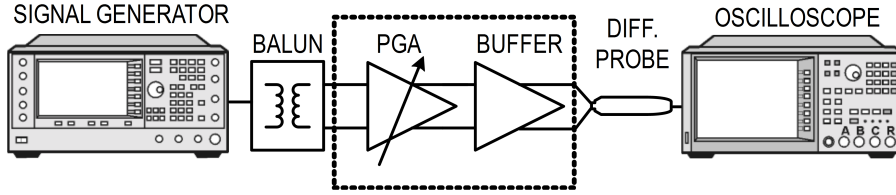


Figure 5.4.1. Measurement setup.

	JSSC-13	TCAS-14	JSSC-15	This work
Technology	65nm	150nm	180nm	180nm
Active Area [mm²]	0.01	0.05	0.07	0.03
Gain Range [dB]	-13 / 63	-5.5 / 28	3.6 / 59.6	15 / 66
dB-linear Gain Range [dB]	50	34	56	51
OP_{1dB} [dBm]	-	5.6	-3	8
OIP3 [dBm]	11.5	13 / 17.3	8	14.3
Input Noise [nV/(Hz)^{0.5}]	3.5	11.14	10.6	10.7
Bandwidth [MHz]	14.8	60	63.5	50
GBW [GHz]	21	1.5	60.6	100
N of stages	3	1	15	1
Power [mW]	2.16	7.56	1.12	0.42

Table 5.4.1. Performance summary and comparison.

should have a variation of less than 0.7 dB to be competitive with our solution, difficult to achieve without compensation techniques.

5.4. Experimental Results

For testing purposes, a buffer follows the PGA to drive the measurement instrumentation. Fig. (5.4.1) shows the measurement setup. A signal source and a discrete balun provide the differential input signal while the PGA output is recorded with a scope for post-processing.

Typical screen-shots showing the input and output signals with the PGA operated at two gain settings (20 dB and 60 dB) and two different clock frequencies (10 MHz, 100 MHz) are reported in Fig. (5.4.2). The estimated core power dissipation, including control signal generation, rises almost linearly with the clock frequency and, at 100 MHz, it is 420

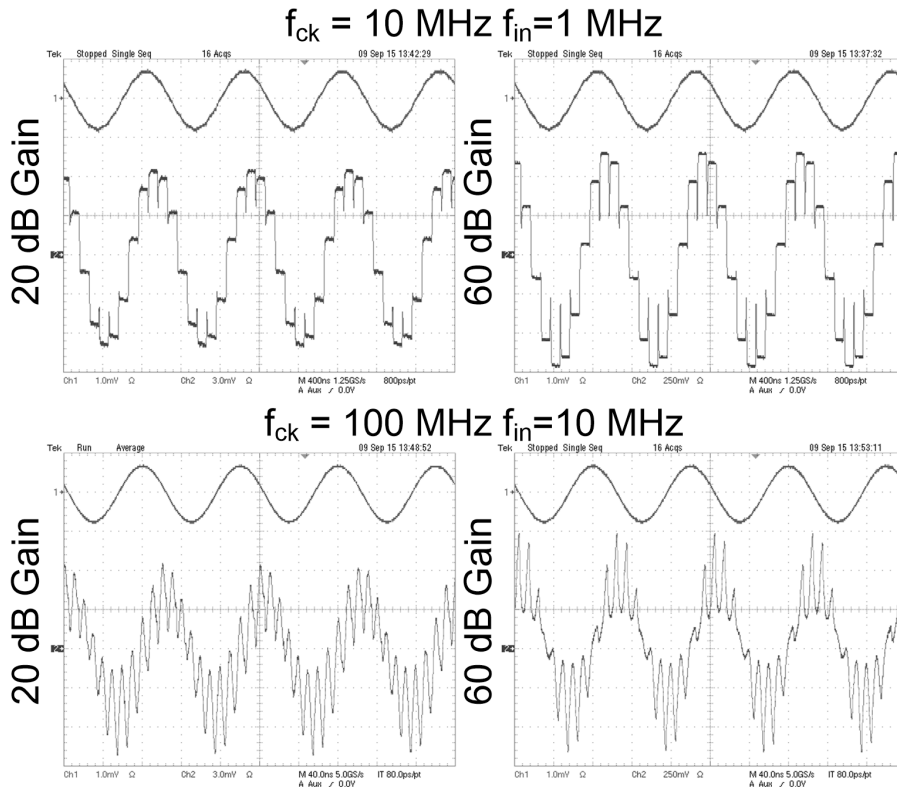


Figure 5.4.2. Scope screenshots showing the PGA input and output signals.

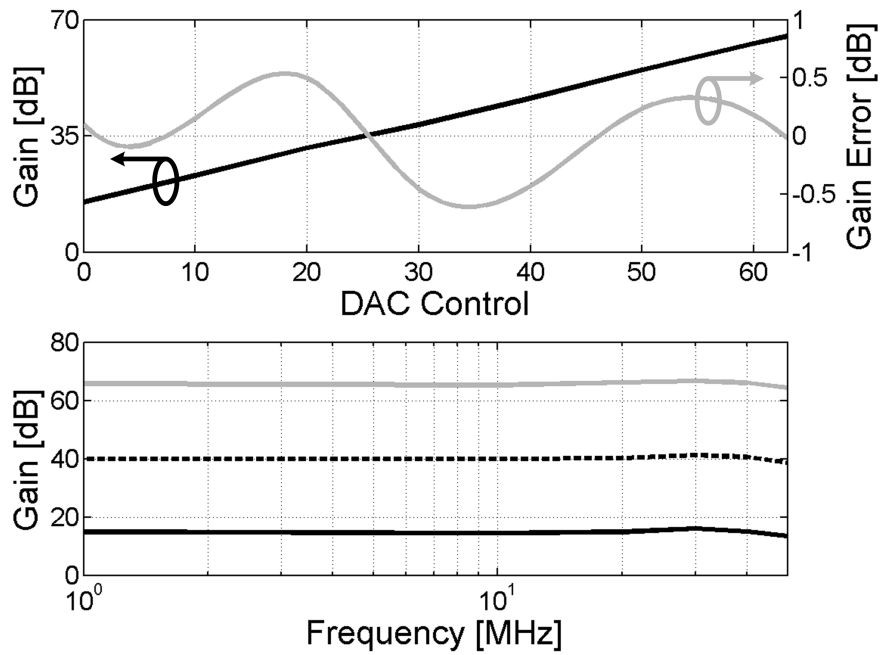


Figure 5.4.3. Measured gain and frequency response.

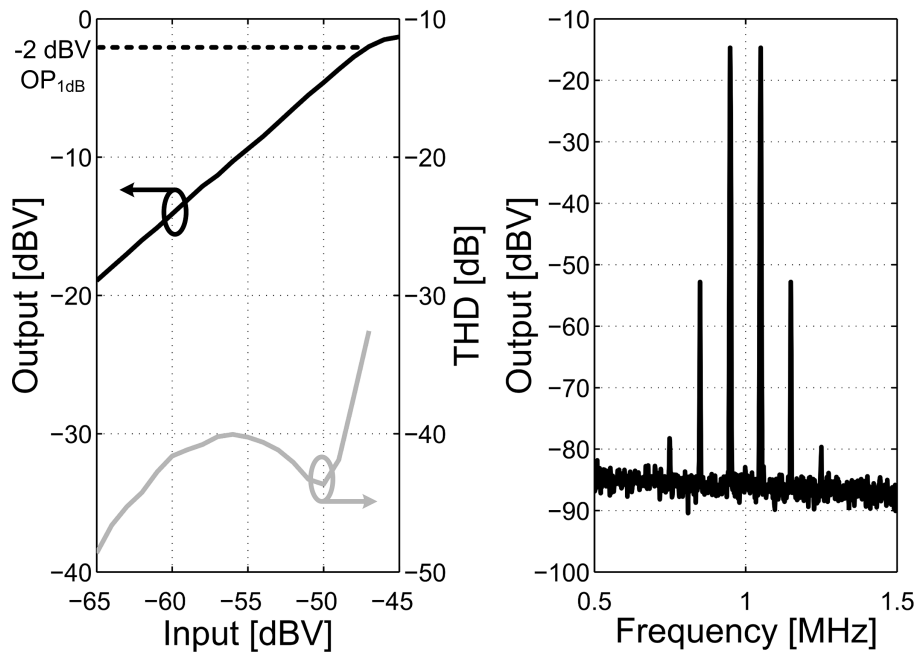


Figure 5.4.4. Gain compression, THD and IM3 test.

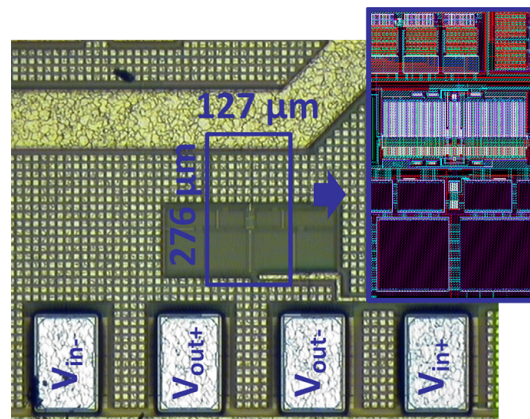


Figure 5.4.5. Chip photograph.

μW from $V_{dd}=1.8$ V. Measured gain and frequency response with the PGA clocked at 100 MHz are reported in Fig. (5.4.3). By changing the control code of the DAC determining T_{reg} , gain ranges from 15 dB to 66 dB with $\pm 0.6\text{dB}$ maximum deviation from an ideal dB-linear curve. The frequency response shown in the bottom plot is almost flat (less

than 3dB variation) up to 50 MHz and independent from the gain setting. The equivalent input noise power estimated from measurements is $(76 V_{rms})^2$, corresponding to a power spectral density spread over a 50 MHz bandwidth of $10.7 nV/\sqrt{Hz}$. Results from distortion tests are reported in Fig. (5.4.4). The left plot shows the input-output curve and THD at 45 dB gain. Output 1dB gain compression point, OP1dB, is -2 dBV (8 dBm on a 50 load). THD at OP1dB is -32 dB and better than -40 dB from 10dB back-off down. The right plot shows the result of an IM3 test with two sidebands of -14.7 dBV separated by 100 kHz. The IM3 is 38.1 dB below the main tones, corresponding to an equivalent OIP3 of 4.3 dBV (14.3 dBm). Finally, the performance of the PGA is summarized in the table (5.4.1), together with state-of-the-art amplifiers featuring similar bandwidth and dB-linear gain control. Noise and distortion are comparable or better than other designs. One design [51] in 65nm CMOS shows lower noise but bandwidth is limited to 14.8 MHz and power dissipation is 5x higher. By leveraging regeneration, the proposed PGA is able to drive large load capacitors directly while demonstrating a record GBW of 100 GHz with only 420 μ W power dissipation which is 2.7 times lower than the lowest in the table. A chip photograph is shown in Fig. (5.4.5).

CHAPTER 6

Conclusions

In Chapter 2 and 3, a comparison between the fundamental amplifier configurations for CMUT amplifiers has been proposed. The impact on the pulse-echo frequency response and SNR have been assessed. The study demonstrated that a capacitive-feedback stage provides a remarkable improvement in the noise-power performance compared to the very popular resistive-feedback amplifier, at the expense of a low-frequency shift of the pulse-echo response, making it suitable for integration of dense CMUT arrays for low and mid-frequency ultrasound imaging applications. Moreover, a CMUT transceiver front-end suitable for mobile ultrasound imaging applications in BCD-SOI technology was presented. By leveraging the results of the analysis and through a careful co-design of the RX and TX circuits to mitigate the effects of the large parasitic capacitances introduced by the high voltage transistors, the transceiver is able to deliver up to 100V pulses while featuring an ultra-low power RX amplifier with a record dynamic range and noise FoM. System functionality has been extensively demonstrated with electrical and pulse-echo measurements.

In Chapter 4, a CMUT linearization method, based on the pre-distortion of unipolar digital pulses, was introduced. A pulser circuit topology with trapezoidal pulse shaping capability, suitable for integration, was presented. An IC prototype was fabricated and connected to a CMUT. Experimental results demonstrated a significant reduction

of the secondharmonic distortion, which is estimated to be lower than -30 dB, resulting in good linearization for typical nonlinear imaging operation.

In Chapter 5, the performance of the cross-coupled pair has been investigated for discrete-time linear amplification. Its regeneration feature proved to be attractive for designing CMOS PGAs, enabling accurate dB-linear gain control and very high gain-bandwidth product (GBW) at low power. A test-chip in 0.18 μm CMOS provided 15dB to 66dB gain over 50MHz bandwidth. With state-of-the art noise and linearity performances, a record GBW up to 100GHz has been demonstrated with only 420 μW power dissipation.

Future work will be devoted to the development of a fully integrated 256-channel analog front-end IC, based on the proposed pulser topology and a receive LNA topology previously presented [21, 22], to be integrated in a 256- element 2D spiral array configuration [59] using CMUT reverse fabrication approach [60].

Bibliography

- [1] A. Savoia, G. Caliano, and M. Pappalardo, “A CMUT probe for medical ultrasonography: from microfabrication to system integration,” *IEEE Transactions on Ultrasonics, Ferroelectrics and Frequency Control*, vol. 59, no. 6, pp. 1127–1138, Jun. 2012.
- [2] A. Savoia, G. Caliano, B. Mauti, and M. Pappalardo, “Performance optimization of a high frequency CMUT probe for medical imaging,” in *Ultrasonics Symposium (IUS), 2011 IEEE International*, Oct. 2011, pp. 600–603.
- [3] L. F. Goncalves, J. Espinoza, J. P. Kusanovic, W. Lee, J. K. Nien, J. Santolaya-Forgas, G. Mari, M. C. Treadwell, and R. Romero, “Applications of 2-dimensional matrix array for 3- and 4-dimensional examination of the fetus: a pictorial essay,” *Journal of Ultrasound in Medicine: Official Journal of the American Institute of Ultrasound in Medicine*, vol. 25, no. 6, pp. 745–755, Jun. 2006.
- [4] L. F. Goncalves, W. Lee, J. Espinoza, and R. Romero, “Three- and 4-dimensional ultrasound in obstetric practice: does it help?” *Journal of Ultrasound in Medicine: Official Journal of the American Institute of Ultrasound in Medicine*, vol. 24, no. 12, pp. 1599–1624, Dec. 2005.
- [5] G.-d. Kim, C. Yoon, S.-B. Kye, Y. Lee, J. Kang, Y. Yoo, and T.-K. Song, “A single FPGA-based portable ultrasound imaging system for point-of-care applications,” *IEEE Transactions on Ultrasonics, Ferroelectrics, and Frequency Control*, vol. 59, no. 7, pp. 1386–1394, Jul. 2012.
- [6] J. Baran and J. Webster, “Design of low-cost portable ultrasound systems: Review,” in *Annual International Conference of the IEEE Engineering in Medicine and Biology Society, 2009. EMBC 2009*, Sep. 2009, pp. 792–795.
- [7] K. C. Kim, M. J. Kim, H. S. Joo, W. Lee, C. Yoon, T.-K. Song, and Y. Yoo, “Smartphone-based portable ultrasound imaging system: A primary result,” in

- Ultrasonics Symposium (IUS), 2013 IEEE International*, Jul. 2013, pp. 2061–2063.
- [8] G. Gurun, C. Tekes, J. Zahorian, T. Xu, S. Satir, M. Karaman, J. Hasler, and F. Degertekin, “Single-chip CMUT-on-CMOS front-end system for real-time volumetric IVUS and ICE imaging,” *IEEE Transactions on Ultrasonics, Ferroelectrics, and Frequency Control*, vol. 61, no. 2, pp. 239–250, Feb. 2014.
- [9] I. Wygant, N. Jamal, H. Lee, A. Nikoozadeh, O. Oralkan, M. Karaman, and B. Khuri-yakub, “An integrated circuit with transmit beamforming flip-chip bonded to a 2-D CMUT array for 3-D ultrasound imaging,” *IEEE Transactions on Ultrasonics, Ferroelectrics and Frequency Control*, vol. 56, no. 10, pp. 2145–2156, Oct. 2009.
- [10] I. O. Wygant, X. Zhuang, D. T. Yeh, O. Oralkan, A. Sanli Ergun, M. Karaman, and B. T. Khuri-Yakub, “Integration of 2d CMUT arrays with front-end electronics for volumetric ultrasound imaging,” *IEEE transactions on ultrasonics, ferroelectrics, and frequency control*, vol. 55, no. 2, pp. 327–342, Feb. 2008.
- [11] A. Bhuyan, J. W. Choe, B. C. Lee, I. Wygant, A. Nikoozadeh, O. Oralkan, and B. Khuri-Yakub, “Integrated Circuits for Volumetric Ultrasound Imaging With 2-D CMUT Arrays,” *IEEE Transactions on Biomedical Circuits and Systems*, vol. 7, no. 6, pp. 796–804, Dec. 2013.
- [12] X. Xu, H. Venkataraman, S. Oswal, E. Bartolome, and K. Vasanth, “Challenges and considerations of analog front-ends design for portable ultrasound systems,” in *2010 IEEE Ultrasonics Symposium (IUS)*, Oct. 2010, pp. 310–313.
- [13] H.-K. Cha, D. Zhao, J. H. Cheong, B. Guo, H. Yu, and M. Je, “A CMOS High-Voltage Transmitter IC for Ultrasound Medical Imaging Applications,” *IEEE Transactions on Circuits and Systems II: Express Briefs*, vol. 60, no. 6, pp. 316–320, Jun. 2013.
- [14] A. Banuaji and H.-K. Cha, “A 15-V Bidirectional Ultrasound Interface Analog Front-End IC for Medical Imaging Using Standard CMOS Technology,” *IEEE Transactions on Circuits and Systems II: Express Briefs*, vol. 61, no. 8, pp. 604–608, Aug. 2014.

- [15] R. Chebli and M. Sawan, "Fully Integrated High-Voltage Front-End Interface for Ultrasonic Sensing Applications," *IEEE Transactions on Circuits and Systems I: Regular Papers*, vol. 54, no. 1, pp. 179–190, Jan. 2007.
- [16] D. Bianchi, F. Quaglia, A. Mazzanti, and F. Svelto, "A 90vpp 720mhz GBW linear power amplifier for ultrasound imaging transmitters in BCD6-SOI," in *Solid-State Circuits Conference Digest of Technical Papers (ISSCC), 2012 IEEE International*, Feb. 2012, pp. 370–372.
- [17] A. S. Savoia, G. Scaglione, G. Caliano, A. Mazzanti, M. Sautto, and F. Quaglia, "Second-harmonic reduction in CMUTs using unipolar pulsers," in *Ultrasonics Symposium (IUS), 2015 IEEE International*, Oct. 2015, pp. 1–4.
- [18] K. Chen, H.-S. Lee, A. Chandrakasan, and C. Sodini, "Ultrasonic Imaging Transceiver Design for CMUT: A Three-Level 30-Vpp Pulse-Shaping Pulser With Improved Efficiency and a Noise-Optimized Receiver," *IEEE Journal of Solid-State Circuits*, vol. 48, no. 11, pp. 2734–2745, Nov. 2013.
- [19] M. Sambì, D. Merlini, P. Galbiati, E. Bonera, and F. Belletti, "A novel 0.16 μm - 300 V SOIBCD for ultrasound medical applications," in *2011 IEEE 23rd International Symposium on Power Semiconductor Devices and ICs (ISPSD)*, May 2011, pp. 36–39.
- [20] D. Bianchi, F. Quaglia, A. Mazzanti, and F. Svelto, "Analysis and Design of a High Voltage Integrated Class-B Amplifier for Ultra-Sound Transducers," *IEEE Transactions on Circuits and Systems I: Regular Papers*, vol. Early Access Online, 2014.
- [21] M. Sautto, D. Leone, A. Savoia, D. Ghisu, F. Quaglia, G. Caliano, and A. Mazzanti, "A CMUT transceiver front-end with 100-V TX driver and 1-mW low-noise capacitive feedback RX amplifier in BCD-SOI technology," in *European Solid State Circuits Conference (ESSCIRC), ESSCIRC 2014 - 40th*, Sep. 2014, pp. 407–410.
- [22] A. Savoia, G. Caliano, A. Mazzanti, M. Sautto, A. Leone, D. Ghisu, and F. Quaglia, "An ultra-low-power fully integrated ultrasound imaging CMUT transceiver featuring a high-voltage unipolar pulser and a low-noise charge amplifier," in *Ultrasonics Symposium (IUS), 2014 IEEE International*, Sep. 2014, pp. 2568–2571.

- [23] M. Sautto, F. Quaglia, G. Ricotti, and A. Mazzanti, “5.6 A 420uW 100ghz-GBW CMOS Programmable-Gain Amplifier leveraging the cross-coupled pair regeneration,” in *2016 IEEE International Solid-State Circuits Conference (ISSCC)*, Jan. 2016, pp. 98–99.
- [24] H. Azhari, *Basics of Biomedical Ultrasound for Engineers*. John Wiley & Sons, Mar. 2010.
- [25] T. L. Szabo, *Diagnostic Ultrasound Imaging: Inside Out*. Academic Press, 2004.
- [26] K. K. Shung, *Diagnostic Ultrasound: Imaging and Blood Flow Measurements, Second Edition*. CRC Press, Apr. 2015, google-Books-ID: izXpBwAAQBAJ.
- [27] W. P. Mason, *Electromechanical transducers and wave filters*. D. Van Nostrand Co., 1948.
- [28] G. Matrone, A. Savoia, M. Terenzi, G. Caliano, F. Quaglia, and G. Magenes, “A volumetric CMUT-based ultrasound imaging system simulator with integrated reception and u-beamforming electronics models,” *IEEE Transactions on Ultrasonics, Ferroelectrics, and Frequency Control*, vol. 61, no. 5, pp. 792–804, May 2014.
- [29] I. Ladabaum, X. Jin, H. Soh, A. Atalar, and B. Khuri-Yakub, “Surface micromachined capacitive ultrasonic transducers,” *IEEE Transactions on Ultrasonics, Ferroelectrics, and Frequency Control*, vol. 45, no. 3, pp. 678–690, May 1998.
- [30] G. Yaralioglu, A. Ergun, B. Bayram, E. Haeggstrom, and B. T. Khuri-Yakub, “Calculation and measurement of electromechanical coupling coefficient of capacitive micromachined ultrasonic transducers,” *IEEE Transactions on Ultrasonics, Ferroelectrics, and Frequency Control*, vol. 50, no. 4, pp. 449–456, Apr. 2003.
- [31] M. Pappalardo, G. Caliano, A. S. Savoia, and A. Caronti, “Micromachined Ultrasonic Transducers,” in *Piezoelectric and Acoustic Materials for Transducer Applications*, A. Safari and E. K. Akdogan, Eds. Springer US, 2008, pp. 453–478.

- [32] G. Gurun, P. Hasler, and F. Degertekin, "Front-end receiver electronics for high-frequency monolithic CMUT-on-CMOS imaging arrays," *IEEE Transactions on Ultrasonics, Ferroelectrics and Frequency Control*, vol. 58, no. 8, pp. 1658–1668, Aug. 2011.
- [33] M. W. Rashid, C. Tekes, M. Ghovanloo, and F. L. Degertekin, "Design of frequency-division multiplexing front-end receiver electronics for CMUT-on-CMOS based intracardiac echocardiography," in *2014 IEEE International Ultrasonics Symposium*, Sep. 2014, pp. 1540–1543.
- [34] J. Lim, E. F. Arkan, G. Jung, F. L. Degertekin, and M. Ghovanloo, "On-chip reduced wire transceiver for high frequency CMUT imaging system," in *2015 IEEE Biomedical Circuits and Systems Conference (BioCAS)*, Oct. 2015, pp. 1–4.
- [35] T. C. Cheng and T. H. Tsai, "CMOS Ultrasonic Receiver With On-Chip Analog-to-Digital Front End for High-Resolution Ultrasound Imaging Systems," *IEEE Sensors Journal*, vol. 16, no. 20, pp. 7454–7463, Oct. 2016.
- [36] P. Behnamfar, R. Molavi, and S. Mirabbasi, "Transceiver Design for CMUT-Based Super-Resolution Ultrasound Imaging," *IEEE Transactions on Biomedical Circuits and Systems*, vol. 10, no. 2, pp. 383–393, Apr. 2016.
- [37] S.-Y. Peng, M. Qureshi, P. Hasler, A. Basu, and F. Degertekin, "A Charge-Based Low-Power High-SNR Capacitive Sensing Interface Circuit," *IEEE Transactions on Circuits and Systems I: Regular Papers*, vol. 55, no. 7, pp. 1863–1872, Aug. 2008.
- [38] S.-Y. Peng, M. Qureshi, A. Basu, R. Guldiken, F. Degertekin, and P. Hasler, "PS-15 Floating-Gate Based CMUT Sensing Circuit Using Capacitive Feedback Charge Amplifier," in *IEEE Ultrasonics Symposium, 2006*, Oct. 2006, pp. 2425–2428.
- [39] I. Cicek, A. Bozkurt, and M. Karaman, "Design of a front-end integrated circuit for 3d acoustic imaging using 2d CMUT arrays," *IEEE Transactions on Ultrasonics, Ferroelectrics and Frequency Control*, vol. 52, no. 12, pp. 2235–2241, Dec. 2005.

- [40] T. Singh, T. Saether, and T. Ytterdal, "Feedback Biasing in Nanoscale CMOS Technologies," *IEEE Transactions on Circuits and Systems II: Express Briefs*, vol. 56, no. 5, pp. 349–353, May 2009.
- [41] G. Gurun, M. Hochman, P. Hasler, and F. Degertekin, "Thermal-mechanical-noise-based CMUT characterization and sensing," *IEEE Transactions on Ultrasonics, Ferroelectrics, and Frequency Control*, vol. 59, no. 6, pp. 1267–1275, Jun. 2012.
- [42] T. Gabrielson, "Mechanical-thermal noise in micromachined acoustic and vibration sensors," *IEEE Transactions on Electron Devices*, vol. 40, no. 5, pp. 903–909, May 1993.
- [43] P. Behnamfar and S. Mirabbasi, "Design of a high-voltage analog front-end circuit for integration with CMUT arrays," in *2010 IEEE Biomedical Circuits and Systems Conference (BioCAS)*, Nov. 2010, pp. 298–301.
- [44] A. Lohfink and P. C. Eccardt, "Linear and nonlinear equivalent circuit modeling of CMUTs," *IEEE Transactions on Ultrasonics, Ferroelectrics, and Frequency Control*, vol. 52, no. 12, pp. 2163–2172, Dec. 2005.
- [45] S. Zhou, P. Reynolds, and J. Hossack, "Precompensated excitation waveforms to suppress harmonic generation in MEMS electrostatic transducers," *IEEE Transactions on Ultrasonics, Ferroelectrics and Frequency Control*, vol. 51, no. 11, pp. 1564–1574, Nov. 2004. [Online]. Available: <http://ieeexplore.ieee.org/lpdocs/epic03/wrapper.htm?arnumber=1367498>
- [46] A. Novell, M. Legros, N. Felix, and A. Bouakaz, "Exploitation of capacitive micromachined transducers for nonlinear ultrasound imaging," *IEEE Transactions on Ultrasonics, Ferroelectrics, and Frequency Control*, vol. 56, no. 12, pp. 2733–2743, Dec. 2009.
- [47] S. Satir and F. L. Degertekin, "Harmonic reduction in capacitive micromachined ultrasonic transducers by gap feedback linearization," *IEEE Transactions on Ultrasonics, Ferroelectrics, and Frequency Control*, vol. 59, no. 1, pp. 50–59, Jan. 2012.
- [48] S. Menigot, D. Certon, D. Gross, and J.-M. Girault, "Automatic optimal input command for linearization of cMUT output by a temporal target," *IEEE Transactions on Ultrasonics, Ferroelectrics, and Frequency*

- Control*, vol. 61, no. 10, pp. 1742–1753, Oct. 2014. [Online]. Available: <http://ieeexplore.ieee.org/lpdocs/epic03/wrapper.htm?arnumber=6910384>
- [49] A. Novell, M. Legros, J.-M. Gregoire, P. A. Dayton, and A. Bouakaz, “Evaluation of bias voltage modulation sequence for nonlinear contrast agent imaging using a capacitive micromachined ultrasonic transducer array,” *Physics in Medicine and Biology*, vol. 59, no. 17, pp. 4879–4896, Sep. 2014.
- [50] H. K. Oguz, S. Olcum, M. N. Senlik, V. Tas, A. Atalar, and H. Koymen, “Nonlinear modeling of an immersed transmitting capacitive micromachined ultrasonic transducer for harmonic balance analysis,” *IEEE Transactions on Ultrasonics, Ferroelectrics, and Frequency Control*, vol. 57, no. 2, pp. 438–447, Feb. 2010.
- [51] I. Choi, H. Seo, and B. Kim, “Accurate dB-Linear Variable Gain Amplifier With Gain Error Compensation,” *IEEE Journal of Solid-State Circuits*, vol. 48, no. 2, pp. 456–464, Feb. 2013.
- [52] H. Liu, X. Zhu, C. Boon, and X. He, “Cell-Based Variable-Gain Amplifiers With Accurate dB-Linear Characteristic in 0.18 um CMOS Technology,” *IEEE Journal of Solid-State Circuits*, vol. 50, no. 2, pp. 586–596, Feb. 2015.
- [53] R. Onet, M. Neag, I. Kovacs, M. Topa, S. Rodriguez, and A. Rusu, “Compact Variable Gain Amplifier for a Multistandard WLAN/WiMAX/LTE Receiver,” *IEEE Transactions on Circuits and Systems I: Regular Papers*, vol. 61, no. 1, pp. 247–257, Jan. 2014.
- [54] B. Razavi, “The Cross-Coupled Pair - Part II [A Circuit for All Seasons],” *IEEE Solid-State Circuits Magazine*, vol. 6, no. 4, pp. 9–12, 2014.
- [55] —, “The Cross-Coupled Pair - Part I [A Circuit for All Seasons],” *IEEE Solid-State Circuits Magazine*, vol. 6, no. 3, pp. 7–10, 2014.
- [56] —, “The Cross-Coupled Pair?Part III [A Circuit for All Seasons],” *IEEE Solid-State Circuits Magazine*, vol. 7, no. 1, pp. 10–13, 2015.
- [57] T. Sepke, P. Holloway, C. G. Sodini, and H. S. Lee, “Noise Analysis for Comparator-Based Circuits,” *IEEE Transactions on Circuits and Systems I: Regular Papers*, vol. 56, no. 3, pp. 541–553, Mar. 2009.
- [58] P. Pala-Schonwalder, F. X. Moncunill-Geniz, J. Bonet-Dalmau, F. del Aguila-Lopez, and R. Giralt-Mas, “Baseband Superregenerative Amplification,” *IEEE*

- Transactions on Circuits and Systems I: Regular Papers*, vol. 56, no. 9, pp. 1930–1937, Sep. 2009.
- [59] A. Ramalli, E. Boni, A. S. Savoia, and P. Tortoli, “Density-tapered spiral arrays for ultrasound 3-D imaging,” *IEEE Transactions on Ultrasonics, Ferroelectrics, and Frequency Control*, vol. 62, no. 8, pp. 1580–1588, Aug. 2015.
- [60] A. Bagolini, A. S. Savoia, A. Picciotto, M. Boscardin, Pierluigi Bellutti, N. Lamberti, and G. Caliano, “PECVD low stress silicon nitride analysis and optimization for the fabrication of CMUT devices,” *Journal of Micromechanics and Microengineering*, vol. 25, no. 1, p. 015012, 2015. [Online]. Available: <http://stacks.iop.org/0960-1317/25/i=1/a=015012>